THE ASTROPHYSICAL JOURNAL, 390:387–404, 1992 May 10

THE LYMAN FOREST OF 0014+813[1]

M. RAUCH AND R. F. CARSWELL
Institute of Astronomy, Madingley Road, Cambridge CB3 0HA, U.K.
F. H. CHAFFEE[2] AND C. B. FOLTZ
Multiple Mirror Telescope Observatory, University of Arizona, Tucson, AZ 85721
J. K. WEBB
School of Physics, University of New South Wales, P.O. Box 1, Kensington 2033, N.S.W., Australia
R. J. WEYMANN
Observatories of Carnegie Institution of Washington, 813 Santa Barbara Street, Pasadena, CA 91101
J. BECHTOLD
Steward Observatory, University of Arizona, Tucson, AZ 85721
AND
R. F. GREEN
National Optical Astronomy Observatories,[3] Box 26732, Tucson, AZ 85726
Received 1991 August 1; accepted 1991 November 18

ABSTRACT

The results of 23 km s^{-1} resolution echelle spectroscopy of the Lyman forest region of the $z = 3.38$ QSO 0014+813 are described. Voigt profile fits to the Lyman series absorption lines yield H I column density and Doppler parameter distributions similar to those obtained in three previous studies of other objects. There is no evidence so far of significant changes of the behavior of these distributions with redshift, except for the number of systems per unit redshift which, for log N(H I) > 13.75 (cgs), is proportional to $(1 + z)^{2.1 \pm 0.5}$. We find no evidence for a correlation between the Doppler parameter and column density and show that an apparent correlation is due entirely to selection effects of line detection and fitting. While the Lyman forest systems as a whole show no clustering, there appears to be a population of weak, narrow-lined systems which show clustering on scales of $\lesssim 1000$ km s^{-1}. It is not clear if these are unidentified heavy element lines or a genuine Lyman forest component. A simple test for voids along the sight line to 0014+813 proved negative. However, applying the same test to the spectrum of 0420−388 reveals a 24 Mpc region where the line number density is significantly below the mean. The depletion is unlikely to be due to a single nearby ionization source.

Subject headings: integalactic medium — quasars: absorption lines — quasars: individual (0014+813)

1. INTRODUCTION

The profusion of absorption lines detected shortward of QSO Lyα emission lines, the Lyman forest, has received enormous attention in recent years, and yet the true nature of these lines still remains unclear. Many valuable phenomenological details have emerged from the fairly large body of intermediate-resolution data in the literature, resulting in some fascinating and fundamental discoveries (see, e.g., Wolfe, 1991 for a review). Nevertheless the spectral resolution of most of these data is too low to resolve individual absorption features, which hampers attempts to derive some of the important physical characteristics of the absorbing clouds.

There are still few QSO spectral studies where the signal-to-noise ratio (S/N), resolution, and wavelength coverage are all sufficient to permit the use of profile-fitting techniques to estimate absorption-line parameters for a large sample of clouds. Early high-resolution data proved valuable in allowing estimates to be made of the physical properties of a few individual absorption systems (Carswell et al. 1984; Chaffee et al. 1985), but limited wavelength coverage precluded the assembly of adequate statistical information for a large ensemble of clouds over a wide range of redshifts. Extensive wavelength coverage at high resolution of two high-redshift objects, 0420−388 (Atwood, Baldwin, & Carswell 1985) and 2000−330 (Carswell et al. 1987) allowed considerable progress to be made, leading to Doppler parameter estimates of typically 30 km s^{-1} and power-law fits to the H I column density distribution. However, the resolution and S/N of these studies did not allow a study of the spread in Doppler widths in particular, since the error estimates were comparable to the spread in values.

This background led us to attempt the higher S/N study described here, in order to reduce analysis problems associated with line blending and to derive better estimates of the column density and Doppler width distributions of Lyman forest clouds. The Doppler widths are of particular interest since they provide upper limits to the cloud temperatures (see Pettini et al. 1990 and Carswell et al. 1991 for recent discussions). In addition, we wish to examine their spatial distribution and number evolution with redshift. To this end, we have selected 0014+813 for detailed study at high spectral resolution, a high redshift ($z_{em} = 3.38$) QSO which is sufficiently bright ($m_v = 16.5$) that data may be collected in a reasonable amount of observing time. Studies to this object at low resolution

[1] Observations upon which this paper is based were obtained with the 4 m Mayall Telescope at Kitt Peak National Observatory.

[2] Senior Visiting Fellow, Institute of Astronomy, 1990 July 1–1991 August 1.

[3] Operated by the Association of Universities for Research in Astronomy (AURA) Inc. under a cooperative agreement with the National Science Foundation.

revealed that it has a rich Lyα absorption spectrum (Kühr et al. 1983; Sargent, Steidel, & Boksenberg 1989). The heavy element systems have been investigated at intermediate resolution (Sargent, Boksenberg, & Steidel 1988, hereafter SBS; Khare, York, & Green 1989) and small regions of the spectrum studied at high resolution (Chaffee et al. 1985, 1986).

2. OBSERVATIONS AND REDUCTIONS

Echelle spectra of 0014+813 were obtained on the Kitt Peak National Observatory 4 m telescope using the Intensified CCD detector system on the nights of 1986 October 26–28. The total exposure time distributed over the three nights was 17.8 hr. On the first night the transparency was good, the seeing about 1".3, and the on-source exposure time 7.2 hr. The two subsequent nights were affected by clouds, and the seeing ranged from 1".2 to 1".9. The spectral coverage was from 4060 to 5345 Å, with an average full width at half-maximum (FWHM) resolution of 23 km s^{-1}.

2.1. *Generation of the Summed Spectrum*

The data for each integration were liberally sprinkled with cosmic rays, and each of these was flagged and the region containing it given zero weight in the individual frames. Most were recognized by a combination of thresholding and comparison with local means. Each frame was then checked and the weaker cosmic-ray events which had been missed removed interactively. Bad columns in the detector were also given zero weight in each frame. Bias subtraction and flat-field corrections were applied in the usual way. The sky-subtracted object spectra were extracted for each frame using a variant of the optimal technique described by Horne (1986), and an error estimate (based on Gaussian statistics using 23 data numbers per photon—see below) was retained. Comparison spectra were obtained immediately before and immediately after each object exposure and were extracted using the same spatial weights as for the object. Wavelength calibration was performed using the sum of these extracted comparison spectra after checking that no significant shifts had occurred during an integration.

Since wavelength shifts from night to night were significant, the data were rebinned onto a linear wavelength scale prior to forming the final summed spectrum for each echelle order. The bin size was chosen to be close to that of the original pixel size in the highest echelle order, and the sum for each order was obtained from the variance-weighted addition of individual extracted spectra. Flagged values under cosmic rays on the original frame were given zero weight in the sum. Comparison spectra were summed using the same weights at the object spectra, and the instrumental profile was determined from local comparison lines. The FWHM of the lines ranged from 26.6 km s^{-1} at 4100 Å, through a minimum of 20.5 km s^{-1} in the range 4700–4900 Å, to 23.0 km s^{-1} at 5300 Å. The comparison line profiles are adequately approximated as Gaussians of the appropriate widths.

As a check on the statistical properties of the data, two partial sums of the spectra were formed, one using the first, third, fifth, etc. exposure on the object, and the other using even-numbered exposures. The difference spectrum of these two was then examined. It consisted of fluctuations about a mean level close to zero, as expected, with a standard deviation a factor of about 1.8 less than that expected from a normal approximation to photon statistics for 23 data numbers per photon. Since the data were recorded using an intensified CCD where signal from a photon event at the back of the intensifier stage is likely to fall on more than one CCD pixel, neighboring pixels will not be statistically independent. Also, the need to rebin the data to compensate for small wavelength shifts introduces some additional correlation between neighboring pixels in the reduced spectrum. As a result the fluctuations in the difference spectrum should indeed be smaller than those based on the assumption of statistically independent data in each wavelength bin.

There is an independent way to estimate the factor by which the standard deviation in the smoothed data should differ from that of the same data recorded in statistically independent bins. A measure of the degree of smoothing was obtained by determining the number of maxima in the data per bin in the difference spectrum, and comparing this result with those obtained by Gaussian-filter smoothing uncorrelated artificial data by various amounts. The results were consistent with 23 data numbers per detected photon and a standard deviation scale factor of 1.8, so these were adopted for subsequent analysis.

The procedure described above may seem unnecessarily detailed, but an understanding of the behavior of the errors is important for various parts of the analysis of the absorption line spectrum.

Regions of the spectrum used to define the continuum were chosen by comparing deviations from trial continua against those expected from photon statistics; the significance of possible absorption features was assessed by comparing the total deviation of a candidate line with that expected from the standard deviation calculated over the line width; and values of χ^2 for profile fits to the lines were used to assess the goodness of fit, and so the number of components required to satisfactorily fit each blend. For all of these the effects on the significance levels of the effective smoothing of the data were taken into account by use of the standard deviation scale factor where appropriate.

The wavelength-dependent instrumental response was removed from each order using observations of the white dwarf L745-46A, whose data were extracted in the same way as those of the object. The flux scaling factor at each wavelength was found by interpolating among tabulated flux values. After this correction was applied, the individual orders were concatenated, using variance-weighting in the overlapping wavelength regions, to yield the spectrum shown in Figure 1. The S/N varies along the spectrum and is significantly poorer at the ends of the wavelength range than in the middle. Its values per 0.11 Å channel in the continuum are ~4.3 at 4100 Å, ~16.5 at 4700 Å, and 5.5 at 5300 Å. The 1 σ wavelength precision of the final summed spectrum is 35 mÅ.

As expected, the strong absorption lines in the object spectrum have central intensities indistinguishable from zero over most of the wavelength range. One strong blend at 5253 Å has a central intensity ~3 σ below zero, but the spectral region above 5200 Å containing this line was in a very noisy part of the detector, and it is quite likely that not all of the numerous noise events in that region were removed properly.

The continuum was fitted using the method described by Carswell et al. (1991), and the absorption lines were measured against this continuum using the procedure described by Young et al. (1979).

2.2. *Determination of Absorption-Line Parameters*

To determine redshifts (z), Doppler widths ($b = 2^{1/2}\sigma$), and the column densities (N) for ions with observed lines, Voigt

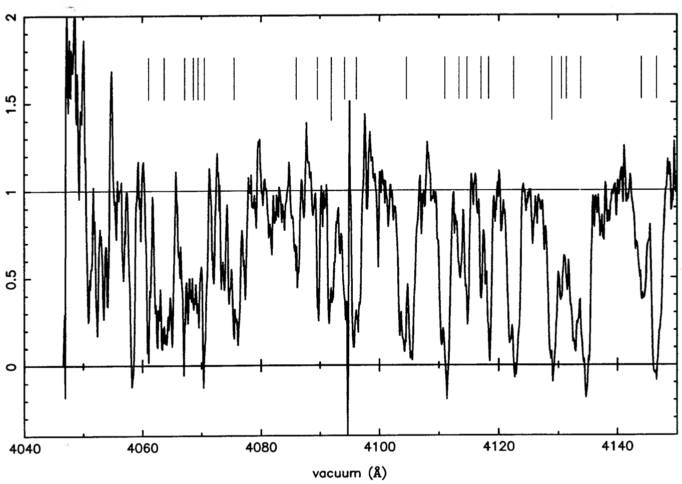

FIG. 1*a*

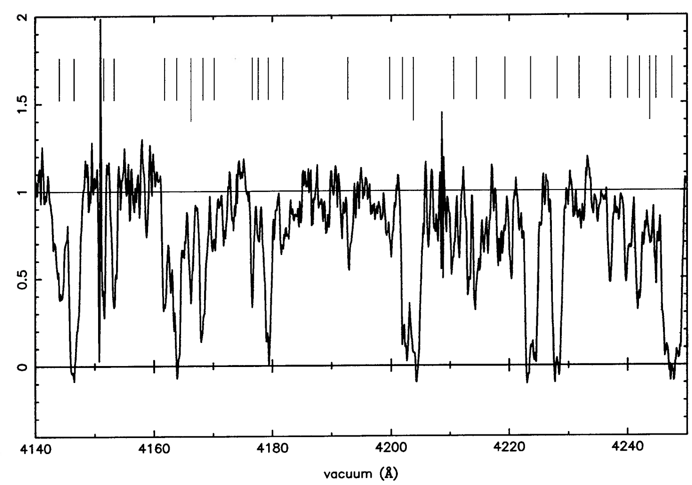

FIG. 1*b*

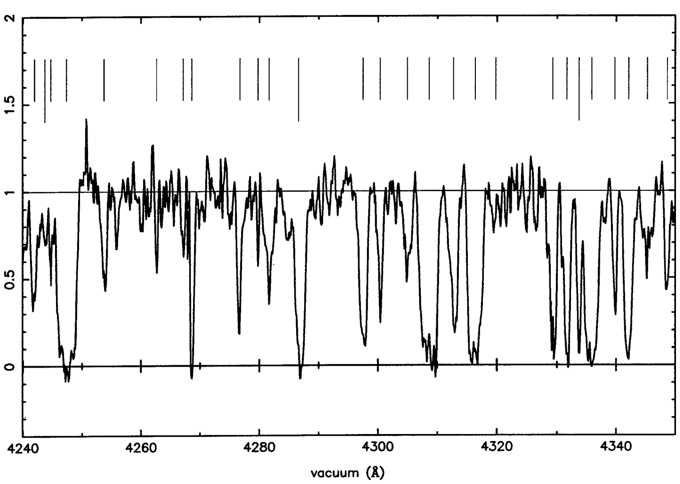

FIG. 1*c*

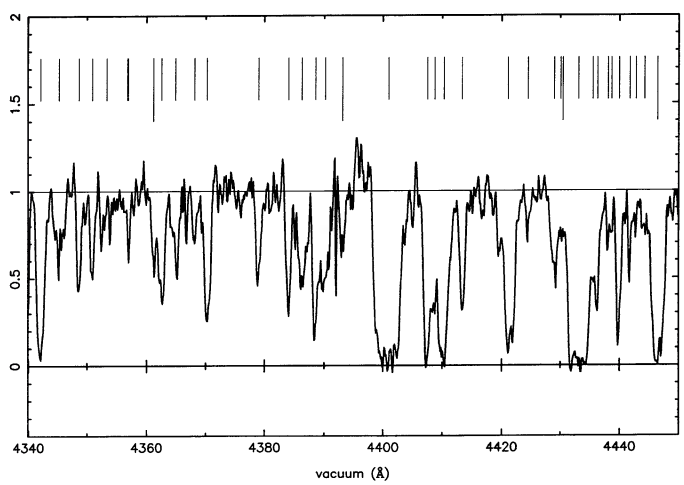

FIG. 1*d*

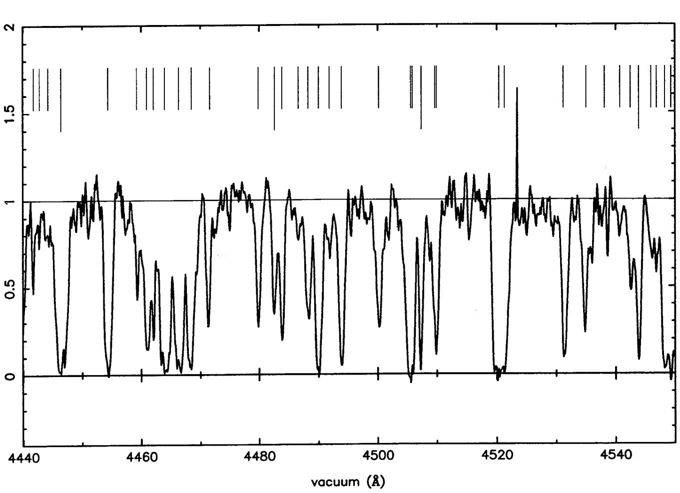

FIG. 1*e*

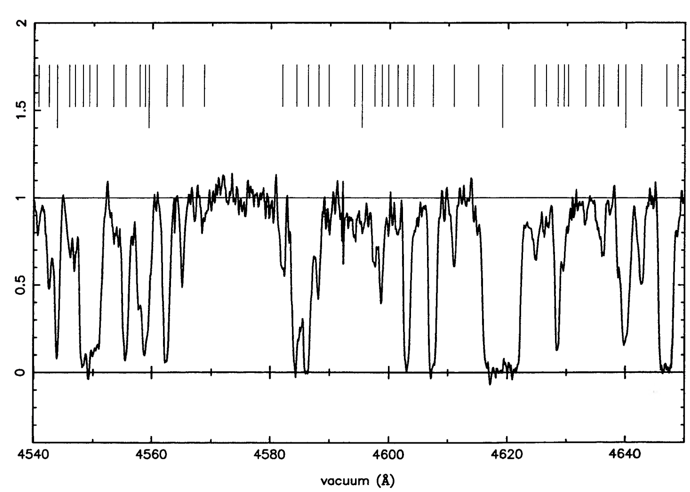

FIG. 1*f*

FIG. 1.—The spectrum of 0014+813 normalized to unit continuum. The tick marks show the position of the numbered components given in Table 1. There are a number of noise spikes in the spectrum (notably at ~4095, 4151, 4209, and 4523 Å) due to detector defects.

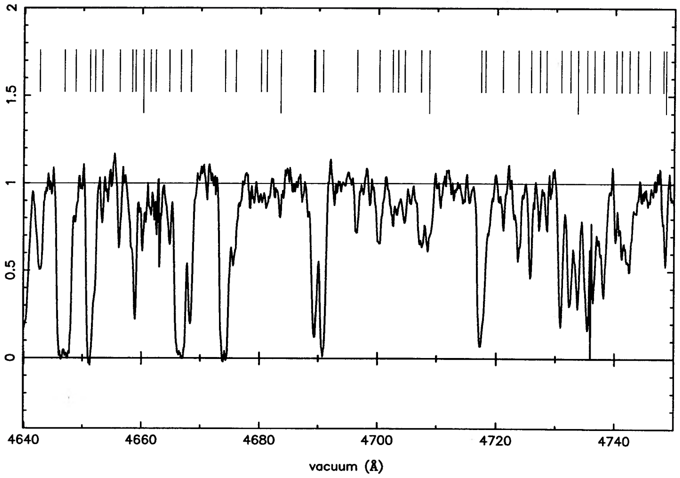

FIG. 1*g*

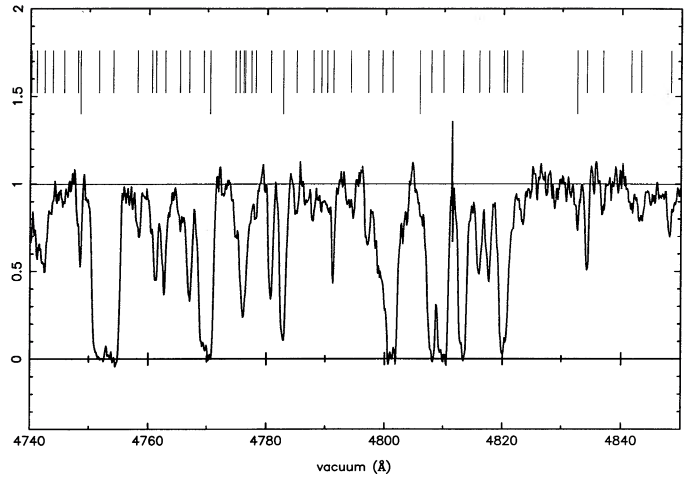

FIG. 1*h*

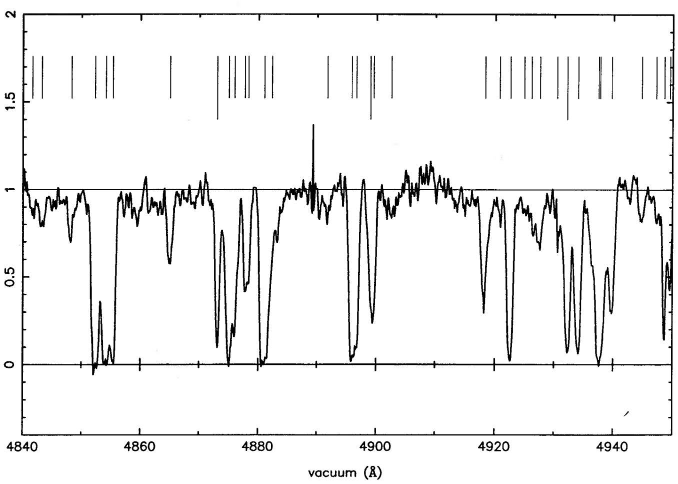

FIG. 1*i*

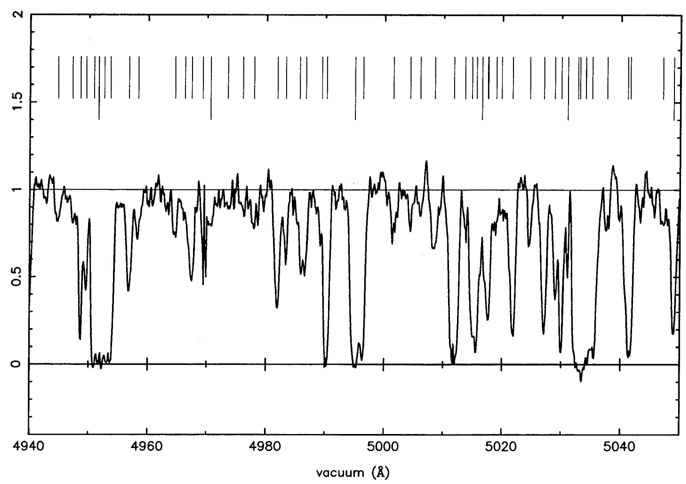

FIG. 1*j*

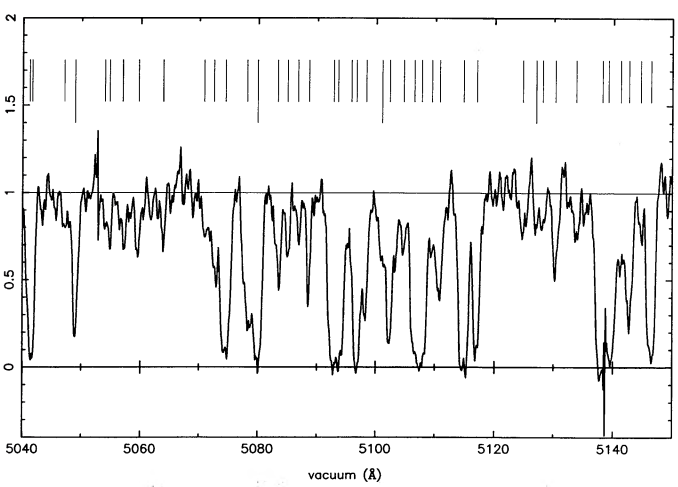

FIG. 1*k*

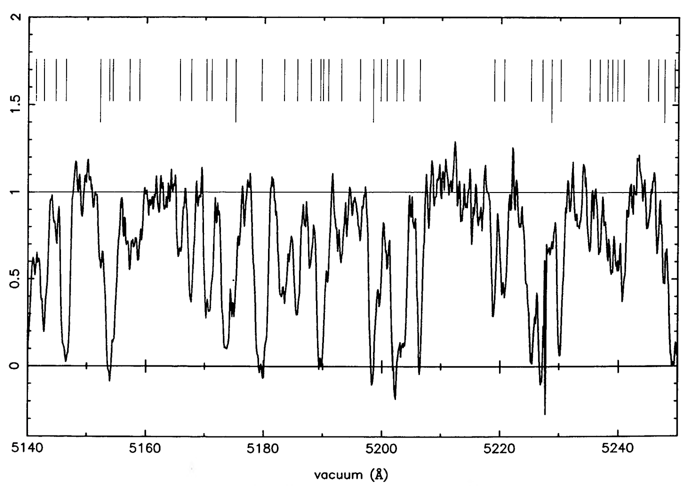

FIG. 1*l*

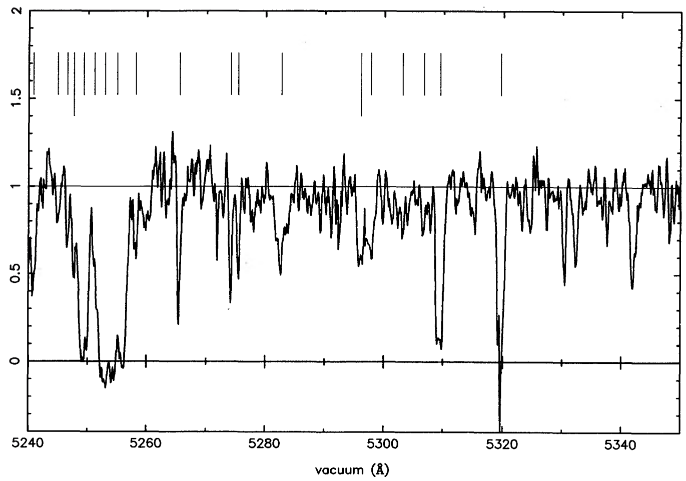

FIG. 1*m*

profiles convolved with a Gaussian of the appropriate instrumental width were fitted to the lines using the technique described by Carswell et al. (1987).

The number of components fitted to each blend was determined by a procedure (Carswell et al. 1991) in which the reduced χ^2 value ($=\chi^2$ divided by the number of degrees of freedom, ν) for the best fit is calculated as a function of the number of line components used. For a 7.15 Å (65 channel) window near 5073 Å, Figure 2 illustrates the typical behavior of χ^2/ν with ν as the number of components (each of which expends 3 degrees of freedom—b, N, and z) is increased. It can be seen that the reduced χ^2 is a steep function of the number of components used in the fit. The final number of components used to fit each blend was the minimum number required to achieve a probability of ≥ 0.01 that the observed χ^2 arose by chance.

It should be pointed out that the reduced χ^2 is not a sensitive indicator of overfitting. In the example shown in Figure 2, the curve descends steeply until three components have been included (leaving 56 degrees of freedom out of the original 65). After a shallow minimum, the χ^2/ν recovers slowly; at lower ν, the $1/\nu$ dependence is felt and χ^2 itself decreases only slowly with the addition of further components.

However, as too many components are introduced (the transition from the steep to the flat part of Fig. 2), the parameter error estimates grow rapidly, so absorption features which have been overfitted are generally identifiable. As a final check, all fitted profiles were examined by eye during the analysis to verify that they appeared consistent with the data. Table 1 gives the results of this procedure for all identified absorption lines. Lines for which equivalent widths are not given are members of unresolved blends, and the equivalent width of the entire blend is quoted for the first line in the group. Figure 3 shows some sample fits to the data.

All fitted lines were assumed to be Lyα except for higher order Lyman lines or confirmed heavy element lines. Because of possible confusion by high-order Lyman lines, only Lyman forest systems with redshifts $z > 2.695$ (in which Lyα absorption is longward of the QSO Lyβ emission) were analyzed. When higher order Lyman lines of a given system were sufficiently unblended, they were fitted simultaneously with the Lyα lines to provide additional constraints on b, N(H I), and z. However, the decision of whether or not to include Lyβ or Lyγ was somewhat subjective and depended on the degree of blending.

3. HEAVY-ELEMENT SYSTEMS

Since the spectral coverage did not include any region outside the Lyman forest, there is little new information on heavy-element systems. However, because the resolution used here is higher than in previous studies of this object (cf. Chaffee

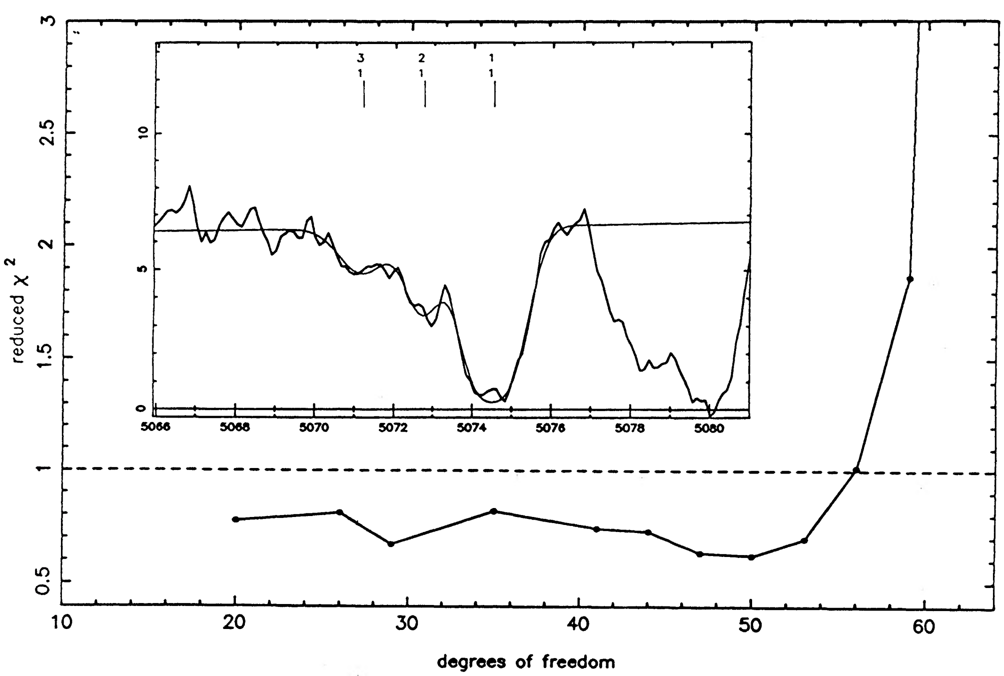

FIG. 2.—Reduced χ^2 vs. number of degrees of freedom ν. The region fitted is shown in the inset with the best fit by three components. Each dot in the main diagram corresponds to a fit with (65-ν)/3 components.

TABLE 1

0014+813 ABSORPTION-LINE PARAMETERS

n	λ_{vac} (A)	±	EW	±	ID	z
1	4061.08	0.08	0.73	0.13		
2	4063.72	0.10	2.65	0.22		
3	4067.17	0.09	1.32	0.17		
4	4068.62	0.04	0.47	0.08		
5	4069.43	0.04	0.55	0.08		
6	4070.49	0.05	0.87	0.10		
7	4075.49	0.10	2.42	0.19		
8	4085.96	0.11	0.51	0.10		
9	4089.60	0.10	0.45	0.09		
10	4091.93	0.07	0.85	0.10		
11	4094.15	0.01	1.00	0.01		
12	4096.09	0.05	1.22	0.09		
13	4104.55	0.08	2.55	0.14		
14	4111.00	0.05	1.90	0.11		
15	4113.35	0.08	0.47	0.08		
16	4114.67	0.05	0.56	0.07		
17	4117.02	0.07	0.39	0.07		
18	4118.32	0.05	0.93	0.08		
19	4122.50	0.04	2.09	0.10		
20	4128.90	0.05	1.80	0.10		
21	4130.51	0.03	0.52	0.05		
22	4131.34	0.03	0.27	0.04		
23	4133.78	0.05	3.34	0.11		
24	4144.05	0.08	1.10	0.10		
25	4146.53	0.04	1.88	0.10		
26	4151.50	0.03	0.43	0.05		
27	4153.27	0.05	0.58	0.07		
28	4161.82	0.04	0.59	0.06		
29	4163.86	0.05	1.86	0.10		
30	4166.27	0.07	0.56	0.07		
31	4168.27	0.05	1.04	0.08		
32	4170.15	0.12	0.34	0.07		
33	4176.61	0.09	0.39	0.07		
34	4177.64	0.06	0.17	0.04		
35	4179.33	0.06	1.32	0.09		
36	4181.77	0.08	0.34	0.06		
37	4192.74	0.11	0.48	0.08		
38	4199.77	0.10	0.43	0.07		
39	4201.91	0.02	0.46	0.04		
40	4203.74	0.03	2.64	0.09		
41	4210.61	0.12	0.63	0.09		
42	4214.49	0.09	1.52	0.11		
43	4219.26	0.11	0.81	0.09		
44	4223.62	0.05	2.49	0.09		
45	4228.08	0.03	1.84	0.07		
46	4231.81	0.16	0.27	0.07		
47	4237.13	0.07	0.45	0.06		
48	4240.02	0.06	0.57	0.06		
49	4241.99	0.05	0.84	0.07		
50	4243.73	0.06	0.26	0.05		
51	4244.76	0.05	0.30	0.05		
52	4247.41	0.03	3.39	0.08		
53	4253.71	0.06	0.52	0.06		
54	4262.64	0.04	0.22	0.04		
55	4267.13	0.06	0.23	0.05		

n	λ_{vac} (A)	±	EW	±	ID	z
56	4268.62	0.09	0.88	0.16		
57	4276.77	0.06	0.71	0.06		
58	4279.78	0.03	0.14	0.03	ZnII 2026	1.11229
59	4281.61	0.06	0.81	0.07		
60	4286.55	0.06	2.20	0.09		
61	4297.49	0.04	1.33	0.06		
62	4300.36	0.05	0.63	0.06		
63	4304.95	0.09	0.63	0.07		
64	4308.59	0.03	2.97	0.08		
65	4312.64	0.05	1.15	0.07		
66	4316.27	0.03	2.43	0.07		
67	4319.78	0.14	0.26	0.06		
68	4329.27	0.05	1.20	0.10		
69	4331.65	0.03	1.25	0.06		
70	4333.71	0.03	0.75	0.04		
71	4335.83	0.03	2.38	0.06		
72	4339.78	0.05	0.54	0.05		
73	4342.12	0.04	1.51	0.06		
74	4345.28	0.08	0.63	0.06		
75	4348.64	0.04	0.50	0.05		
76	4350.89	0.06	0.42	0.05		
77	4353.34	0.15	0.45	0.07		
78	4356.88	0.14	0.34	0.06	Lyα	2.58387
79					ZnII 2026	1.11229
80	4361.18	0.07	0.37	0.06		
81	4362.56	0.04	0.79	0.05		
82	4364.90	0.07	0.54	0.06		
83	4368.12	0.08	0.26	0.05		
84	4370.21	0.04	0.93	0.06		
85	4379.06	0.06	0.53	0.05		
86	4384.03	0.03	0.63	0.05		
87	4386.27	0.06	0.96	0.06		
88	4388.56	0.02	0.94	0.04		
89	4390.21	0.04	0.87	0.05		
90	4393.14	0.07	0.31	0.05		
91	4400.98	0.04	4.63	0.09		
92	4407.50	0.03	1.48	0.05		
93	4408.73	0.01	0.36	0.03		
94	4410.28	0.03	2.01	0.05		
95	4413.32	0.04	0.73	0.05		
96	4421.10	0.06	2.19	0.07		
97	4424.49	0.09	0.19	0.04		
98	4428.97	0.06	0.67	0.05		
99	4430.08	0.03	0.08	0.02		
100	4430.46	0.03	0.11	0.02		
101	4433.14	0.02	3.96	0.06		
102	4435.52	0.01	0.11	0.01		
103	4436.31	0.03	0.71	0.04		
104	4438.08	0.05	0.20	0.03		
105	4438.71	0.04	0.11	0.02		
106	4439.94	0.03	0.87	0.05		
107	4441.76	0.04	0.30	0.04		
108	4442.76	0.08	0.14	0.03		
109	4444.22	0.04	0.10	0.02		
110	4446.40	0.03	2.36	0.06		

n	λ_{vac} (A)	±	EW	±	ID	z
111	4454.36	0.03	1.50	0.05		
112	4459.23	0.05	0.44	0.04		
113	4460.90	0.02	1.14	0.04		
114	4462.09	0.01	0.51	0.03		
115	4463.97	0.01	2.07	0.04		
116	4466.34	0.01	1.78	0.03		
117	4468.46	0.02	1.59	0.04		
118	4471.61	0.05	0.76	0.05		
119	4479.85	0.04	0.68	0.04		
120	4482.56	0.02	0.55	0.03		
121	4483.81	0.02	0.70	0.03		
122	4486.56	0.06	0.18	0.03		
123	4488.18	0.03	0.80	0.04		
124	4489.97	0.01	1.36	0.03		
125	4491.78	0.05	0.31	0.03		
126	4493.79	0.02	1.15	0.04		

n	λ_{vac} (A)	±	EW	±	ID	z	±	b	±	log N	±
127	4500.14	0.06	1.23	0.06	Lyα	2.70182	0.00003	44	3	13.85	0.03
128	4505.39	0.02	1.96	0.04	Lyα	2.70564	0.00099	64	43	13.69	0.75
129					Lyα	2.70625	0.00003	30	9	14.78	0.34
130	4507.34	0.02	0.82	0.03	Lyα	2.70764	0.00001	19	2	14.00	0.09
131	4509.63	0.03	1.14	0.04	Lyα	2.70916	0.00031	65	21	13.53	0.21
132					Lyα	2.70980	0.00002	25	5	13.85	0.09
133	4520.66	0.02	2.92	0.05	Lyα	2.71840	0.00010	35	5	15.69	0.67
134					Lyα	2.71917	0.00068	51	25	14.10	0.72
135	4531.14	0.04	1.28	0.05	Lyα	2.72749	0.00002	33	2	14.02	0.03
136	4535.04	0.03	0.96	0.04	Lyα	2.73031	0.00003	33	4	13.74	0.04
137	4538.12	0.10	0.22	0.04	CII 1334	2.40095	0.00003	3	13	13.71	2.83
138	4540.69	0.10	0.16	0.03	Lyα	2.73510	0.00006	31	7	12.95	0.08
139	4542.47	0.03	0.51	0.03	Lyα	2.73671	0.00003	39	4	13.57	0.03
140	4543.84	0.01	0.90	0.03	Lyα	2.73776	0.00001	24	2	13.94	0.03
141	4545.87	0.05	0.29	0.03	Lyα	2.73949	0.00015	37	15	13.30	0.15
142	4546.79	0.02	0.25	0.02	Lyα	2.74020	0.00011	18	18	13.12	0.47
143	4549.50	0.02	3.67	0.04	Lyα	2.74132	0.00008	31	5	14.22	0.11
144					Lyα	2.74219	0.00008	27	12	14.22	0.15
145					Lyα	2.74322	0.00009	55	6	14.25	0.06
146	4553.39	0.05	0.19	0.03	Lyα	2.74593	0.00012	54	15	13.30	0.09
147	4555.50	0.03	1.46	0.04	Lyα	2.74737	0.00002	36	3	14.10	0.03
148	4558.64	0.02	1.89	0.04	Lyα	2.74929	0.00019	45	13	13.77	0.17
149					Lyα	2.75003	0.00014	25	14	13.85	0.45
150					Lyα	2.75055	0.00040	33	21	13.67	0.56
151	4562.45	0.03	1.28	0.05	Lyα	2.75301	0.00002	33	2	14.15	0.04
152	4565.12	0.05	0.39	0.04	Lyα	2.75522	0.00003	24	3	13.38	0.04
153	4568.69	0.10	0.15	0.04	Lyα	2.75814	0.00010	33	12	12.90	0.12
154	4582.00	0.04	0.45	0.04	Lyα	2.76917	0.00006	32	7	13.44	0.07
155	4584.33	0.02	1.64	0.04	SiIII 1206	2.79968	0.00005	44	4	13.65	0.06
156	4586.25	0.01	1.57	0.03	SiIII 1206	2.80118	0.00005	46	5	13.72	0.06
157	4588.06	0.03	0.54	0.03	Lyα	2.77413	0.00009	25	7	13.51	0.14
158	4589.75	0.08	0.16	0.03	Lyα	2.77550	0.00014	37	18	12.95	0.14
159	4594.10	0.05	0.20	0.03	Lyα	2.77908	0.00006	22	11	12.94	0.17
160	4595.39	0.07	0.18	0.03	Lyα	2.78028	0.00017	65	29	13.18	0.14
161	4597.52	0.03	0.38	0.03	Lyα	2.78191	0.00005	33	7	13.39	0.07
162	4598.73	0.02	0.53	0.03	Lyα	2.78285	0.00003	24	5	13.51	0.05
163	4599.83	0.04	0.09	0.02	Lyα	2.78370	0.00009	23	13	12.85	0.15
164	4601.42	0.05	0.19	0.03	Lyα	2.78509	0.00006	26	8	13.01	0.09
165	4603.28	0.03	1.48	0.04	Lyα	2.78642	0.00001	25	4	14.45	0.18
166					Lyα	2.78728	0.00048	80	36	13.37	0.25
167	4607.39	0.02	1.57	0.04	Lyα	2.79000	0.00001	30	3	14.64	0.15
168	4610.93	0.06	0.34	0.04	Lyα	2.79295	0.00003	27	4	13.29	0.04

TABLE 1—*Continued*

n	λ_{vac} (A)	±	EW	±	ID	z	±	b	±	log N	±	
169	4618.98	0.02	6.74	0.06	Lyα	2.79629	0.00028	46	30	13.10	0.25	
170					MLyα	2.79958	0.00002	89	4	16.40	0.20	complex?
171	4624.51	0.04	0.53	0.03	Lyα	2.80424	0.00007	39	9	13.26	0.08	
172	4626.42	0.05	0.26	0.03	Lyα	2.80565	0.00017	51	23	13.01	0.15	
173	4628.86	0.03	1.33	0.04	Lyα	2.80734	0.00002	26	2	13.94	0.04	
174					Lyα	2.80816	0.00006	18	10	13.17	0.19	
175					Lyα	2.80880	0.00026	30	29	12.87	0.35	
176	4633.22	0.10	0.11	0.03	Lyα	2.81124	0.00007	23	8	12.75	0.10	
177	4636.01	0.10	0.48	0.04	Lyα	2.81308	0.00019	34	16	13.02	0.22	
178					Lyα	2.81373	0.00007	21	7	13.13	0.16	
179	4639.87	0.02	1.64	0.04	Lyα	2.81576	0.00003	10	6	12.98	0.10	
180					Lyα	2.81680	0.00002	50	2	14.11	0.02	
181	4642.61	0.04	0.61	0.04	Lyα	2.81899	0.00002	37	3	13.57	0.03	
182	4646.92	0.02	2.69	0.04	Lyα	2.82244	0.00001	38	3	15.57	0.28	
183					Lyα	2.82400	0.00006	18	9	12.85	0.12	
184	4651.37	0.02	1.50	0.04	Lyα	2.82600	0.00003	19	5	14.93	0.68	
185					Lyα	2.82672	0.00005	16	5	13.45	0.10	
186	4653.29	0.05	0.10	0.02	Lyα	2.82777	0.00006	8	11	12.75	0.15	
187	4656.25	0.04	0.19	0.03	Lyα	2.83018	0.00004	12	6	13.05	0.08	
188	4658.67	0.03	0.74	0.04	Lyα	2.83194	0.00019	32	14	13.33	0.22	
189					Lyα	2.83240	0.00003	11	5	13.61	0.13	
190	4660.24	0.04	0.29	0.03	Lyα	2.83343	0.00005	35	7	13.26	0.06	
191	4661.45	0.05	0.09	0.02	Lyα	2.83449	0.00008	14	14	12.69	0.20	
192	4662.32	0.05	0.14	0.03	Lyα	2.83526	0.00011	25	19	12.96	0.19	
193	4664.61	0.05	0.27	0.03	Lyα	2.83710	0.00004	24	5	13.15	0.05	
194	4666.56	0.01	2.00	0.03	Lyα	2.83868	0.00001	39	3	14.77	0.12	
195	4668.30	0.02	0.73	0.03	Lyα	2.84009	0.00001	23	2	13.78	0.03	
196	4674.12	0.01	1.76	0.03	Lyα	2.84482	0.00001	29	3	14.76	0.17	
197	4675.91	0.03	0.45	0.03	Lyα	2.84608	0.00007	50	7	13.58	0.05	
198	4680.71	0.13	0.21	0.04	Lyα	2.84985	0.00041	48	72	12.79	0.53	
199					Lyα	2.85077	0.00022	26	23	12.68	0.51	
200	4683.51	0.08	0.12	0.03	Lyα	2.85256	0.00007	23	9	12.81	0.11	
201	4689.19	0.02	1.02	0.03	Lyα	2.85726	0.00071	70	44	13.36	0.63	
202					Lyα	2.85741	0.00004	27	6	13.88	0.15	
203	4690.71	0.01	1.12	0.02	Lyα	2.85857	0.00003	24	3	14.24	0.11	
204	4696.46	0.05	0.21	0.03	Lyα	2.86325	0.00003	21	4	13.07	0.06	
205	4700.21	0.05	0.38	0.03	Lyα	2.86635	0.00004	35	4	13.33	0.04	
206	4702.40	0.07	0.18	0.03	Lyα	2.86819	0.00013	27	13	12.98	0.15	
207	4703.33	0.04	0.12	0.02	Lyα	2.86883	0.00012	13	19	12.57	0.40	
208	4704.42	0.05	0.19	0.02	Lyα	2.86985	0.00013	59	16	13.19	0.09	
209	4707.21	0.04	0.47	0.03	Lyα	2.87216	0.00008	43	8	13.43	0.07	
210	4708.65	0.03	0.42	0.02	Lyα	2.87327	0.00008	38	7	13.38	0.08	
211	4717.57	0.04	1.58	0.04	Lyα	2.88044	0.00003	30	4	14.03	0.12	
212					Lyα	2.88103	0.00039	56	18	13.61	0.31	
213	4720.98	0.09	0.19	0.03	Lyα	2.88349	0.00008	31	9	12.99	0.09	
214	4723.60	0.05	0.46	0.04	Lyα	2.88562	0.00004	38	5	13.42	0.04	
215	4725.73	0.04	0.38	0.03	Lyα	2.88733	0.00002	18	3	13.37	0.04	
216	4727.21	0.07	0.14	0.03	Lyα	2.88855	0.00005	16	7	12.88	0.09	
217	4728.36	0.05	0.14	0.03	Lyα	2.88956	0.00004	9	7	12.87	0.10	
218	4730.86	0.02	0.70	0.03	Lyα	2.89155	0.00001	23	2	13.75	0.03	
219	4732.40	0.01	0.70	0.02	Lyα	2.89283	0.00002	31	3	13.72	0.03	
220	4733.69	0.01	0.65	0.02	Lyα	2.89389	0.00002	28	3	13.66	0.03	
221	4735.26	0.01	0.90	0.02	Lyα	2.89521	0.00014	34	8	13.83	0.22	
222	4736.47	0.01	0.58	0.01	Lyα	2.89605	0.00031	42	22	13.72	0.31	
223	4738.04	0.03	0.77	0.03	SiIV 1393	2.39952	0.00002	32	2	13.48	0.02	

n	λ_{vac} (A)	±	EW	±	ID	z	±	b	±	log N	±
224	4740.18	0.03	0.18	0.02	SiIV 1393	2.40100	0.00002	13	3	12.86	0.05
225	4741.08	0.02	0.33	0.02	Lyα	2.90006	0.00015	45	17	13.46	0.17
226	4742.50	0.03	0.75	0.03	Lyα	2.90105	0.00010	37	10	13.52	0.14
227					Lyα	2.90203	0.00010	22	12	12.75	0.18
228	4745.72	0.12	0.11	0.03	Lyα	2.90372	0.00010	40	12	12.78	0.09
229	4748.36	0.03	0.32	0.02	Lyα	2.90572	0.00015	12	15	12.79	0.35
230					Lyα	2.90609	0.00006	9	7	13.16	0.13
231	4752.78	0.02	4.81	0.04	Lyα	2.90876	0.00006	53	4	14.79	0.09
232					Lyα	2.91060	0.00006	39	4	15.20	0.24
233	4758.10	0.06	0.33	0.03	Lyα	2.91407	0.00007	42	8	13.26	0.06
234	4761.00	0.03	0.68	0.03	Lyα	2.91599	0.00088	39	52	13.16	0.91
235					Lyα	2.91654	0.00011	23	11	13.43	0.48
236	4762.79	0.03	0.70	0.03	Lyα	2.91769	0.00003	36	4	13.62	0.04
237	4765.30	0.05	0.23	0.02	Lyα	2.92004	0.00008	44	11	13.20	0.08
238	4766.87	0.02	0.80	0.03	Lyα	2.92125	0.00002	34	3	13.70	0.03
239	4769.76	0.01	2.62	0.03	Lyα	2.92320	0.00008	47	5	14.23	0.07
240					Lyα	2.92413	0.00005	27	3	14.44	0.15
241	4774.61	0.04	0.20	0.02	FeII 2260	1.11195	0.00004	16	3	14.59	0.18
242					Lyα	2.92764	0.00006	25	7	13.06	0.10
243	4776.14	0.02	1.18	0.04	FeII 2260	1.11228	0.00004	18	12	14.75	0.24
244					Lyα	2.92874	0.00003	41	4	13.90	0.03
245					FeII 2260	1.11269	0.00092	46	222	14.12	2.92
246					FeII 2260	1.11314	0.00111	44	58	14.07	2.81
247					FeII 2260	1.11314	0.00004	15	7	14.49	0.20
248	4778.08	0.06	0.14	0.02	Lyα	2.93013	0.00014	49	16	13.11	0.11
249	4780.66	0.03	0.57	0.03	Lyα	2.93254	0.00002	24	2	13.61	0.03
250	4782.74	0.02	1.10	0.03	Lyα	2.93424	0.00001	30	1	14.03	0.03
251	4784.98	0.06	0.12	0.02	Lyα	2.93607	0.00005	18	7	12.80	0.10
252	4787.87	0.07	0.17	0.03	Lyα	2.93829	0.00015	58	18	13.11	0.10
253	4789.20	0.07	0.12	0.02	Lyα	2.93963	0.00020	26	25	12.71	0.38
254	4790.20	0.05	0.11	0.02	Lyα	2.94054	0.00017	33	36	12.88	0.36
255	4791.24	0.04	0.37	0.03	SiII 1260	2.80128	0.00003	19	4	13.05	0.05
256	4794.17	0.08	0.20	0.03	Lyα	2.94365	0.00013	51	17	13.02	0.11
257	4797.04	0.04	0.35	0.03	Lyα	2.94594	0.00005	25	7	13.23	0.09
258	4800.80	0.03	3.53	0.05	Lyα	2.94799	0.00029	81	22	13.95	0.14
259					Lyα	2.94943	0.00004	43	7	14.71	0.18
260	4805.89	0.08	0.14	0.03	Lyα	2.95379	0.00032	54	25	13.25	0.23
261	4807.85	0.01	1.73	0.03	Lyα	2.95506	0.00003	40	5	14.33	0.04
262	4809.92	0.02	1.94	0.05	Lyα	2.95660	0.00002	30	3	15.06	0.22
263	4813.25	0.03	1.74	0.05	Lyα	2.95929	0.00015	51	55	13.92	1.07
264					Lyα	2.95930	0.00005	24	11	14.59	0.29
265	4815.92	0.03	0.59	0.03	Lyα	2.96154	0.00005	39	5	13.55	0.04
266	4817.58	0.03	0.58	0.03	Lyα	2.96290	0.00004	31	4	13.51	0.05
267	4820.21	0.02	1.97	0.04	Lyα	2.96494	0.00004	42	6	14.22	0.08
268					Lyα	2.96538	0.00042	90	24	13.64	0.30
269	4823.22	0.08	0.24	0.03	Lyα	2.96763	0.00008	28	10	13.00	0.13
270	4832.57	0.09	0.18	0.03	Lyα	2.97524	0.00007	27	8	12.98	0.09
271	4834.15	0.03	0.34	0.02	Lyα	2.97655	0.00002	17	3	13.33	0.04
272	4836.85	0.05	0.10	0.02	Lyα	2.97875	0.00006	16	9	12.73	0.12
273	4841.61	0.09	0.14	0.03	Lyα	2.98269	0.00008	28	12	12.74	0.21
274	4843.24	0.07	0.27	0.03	Lyα	2.98397	0.00006	35	9	13.00	0.13
275	4848.30	0.07	0.34	0.03	Lyα	2.98803	0.00004	28	6	13.06	0.07
276	4852.32	0.02	1.67	0.04	Lyα	2.99154	0.00003	33	4	14.49	0.16
277	4854.64	0.01	2.46	0.03	Lyα	2.99298	0.00006	28	5	14.62	0.13
278					Lyα	2.99396	0.00006	22	4	14.31	0.12

TABLE 1—*Continued*

n	λ_{vac} (A)	±	EW	±	ID	*z*	±	*b*	±	log *N*	±	
279	4865.01	0.05	0.48	0.03	Lyα	3.00189	0.00002	35	2	13.44	0.02	
280	4873.03	0.03	0.87	0.04	Lyα	3.00858	0.00002	23	2	13.86	0.04	
281	4875.38	0.02	2.00	0.04	Lyα	3.01012	0.00009	34	5	14.11	0.12	
282					Lyα	3.01093	0.00016	36	9	13.85	0.18	
283	4878.03	0.03	0.74	0.03	Lyα	3.01237	0.00009	17	7	13.38	0.20	
284					Lyα	3.01287	0.00012	20	9	13.38	0.19	
285	4881.53	0.04	2.37	0.06	Lyα	3.01510	0.00002	33	4	14.60	0.15	
286					Lyα	3.01616	0.00044	88	26	13.69	0.20	
287	4891.72	0.10	0.17	0.03	Lyα	3.02386	0.00006	39	8	12.94	0.06	
288	4896.19	0.01	1.71	0.03	Lyα	3.02723	0.00006	21	3	14.07	0.11	
289					Lyα	3.02789	0.00006	23	4	14.07	0.10	β
290	4899.27	0.03	1.01	0.04	Lyα	3.02984	0.00027	29	12	13.49	0.40	
291					Lyα	3.03032	0.00012	23	6	13.63	0.29	β
292	4902.55	0.14	0.29	0.04	Lyα	3.03274	0.00014	73	16	13.14	0.08	
293	4918.33	0.04	0.89	0.04	Lyα	3.04563	0.00002	35	4	13.65	0.05	
294	4920.77	0.07	0.15	0.02	Lyα	3.04785	0.00008	33	10	12.91	0.10	
295	4922.60	0.02	1.27	0.03	Lyα	3.04925	0.00001	28	1	14.17	0.04	β
296	4924.92	0.06	0.11	0.02	Lyα	3.05158	0.00027	67	34	13.12	0.18	
297	4926.18	0.04	0.25	0.02	Lyα	3.05244	0.00007	5	20	12.54	0.23	
298	4927.60	0.04	0.42	0.03	Lyα	3.05330	0.00010	51	10	13.41	0.08	
299	4930.52	0.06	0.20	0.03	Lyα	3.05634	0.00067	73	65	13.43	0.40	
300	4932.19	0.01	1.26	0.03	Lyα	3.05729	0.00002	27	4	14.01	0.08	β
301	4934.06	0.01	1.24	0.03	Lyα	3.05870	0.00002	33	2	14.09	0.03	β
302	4937.51	0.02	2.18	0.04	Lyα	3.06068	0.00022	46	14	13.45	0.19	β
303					Lyα	3.06179	0.00004	40	4	14.34	0.05	β
304	4939.72	0.02	0.83	0.03	Lyα	3.06334	0.00002	35	3	13.79	0.03	β
305	4944.80	0.08	0.18	0.03	Lyα	3.06753	0.00004	30	5	12.95	0.05	
306	4947.24	0.06	0.11	0.02	Lyα	3.06978	0.00019	43	23	13.03	0.17	
307	4948.58	0.01	0.63	0.02	Lyα	3.07069	0.00003	14	4	13.68	0.08	
308	4949.55	0.02	0.42	0.02	Lyα	3.07143	0.00005	24	6	13.46	0.06	
309	4952.32	0.02	3.88	0.04	FeII 2344	1.11195	0.00004	16	3	14.59	0.18	
310					FeII 2344	1.11228	0.00004	18	12	14.75	0.24	
311					FeII 2344	1.11269	0.00092	46	222	14.12	2.92	
312					FeII 2344	1.11314	0.00111	44	58	14.07	2.81	
313					FeII 2344	1.11314	0.00004	15	7	14.49	0.20	
314	4956.74	0.04	0.67	0.04	Lyα	3.07741	0.00002	33	2	13.59	0.02	
315	4958.33	0.05	0.26	0.03	SiII 1304	2.80128	0.00003	19	4	13.05	0.05	
316	4964.60	0.06	0.24	0.03	Lyα	3.08380	0.00004	24	5	13.08	0.06	
317	4967.15	0.05	0.75	0.04	Lyα	3.08520	0.00030	43	28	12.99	0.29	
318					Lyα	3.08616	0.00006	32	5	13.52	0.08	
319	4969.26	0.03	0.20	0.03	Lyα	3.08784	0.00008	22	6	13.28	0.14	
320	4970.61	0.15	0.46	0.08	Lyα	3.08878	0.00015	43	16	13.15	0.14	
321	4973.53	0.11	0.11	0.03	Lyα	3.09121	0.00016	42	19	12.79	0.15	
322	4976.03	0.09	0.12	0.03	Lyα	3.09329	0.00013	30	15	12.77	0.15	
323	4977.91	0.07	0.28	0.03	Lyα	3.09484	0.00010	46	11	13.14	0.08	
324	4981.84	0.02	0.70	0.03	Lyα	3.09803	0.00002	29	2	13.68	0.03	
325	4983.28	0.04	0.32	0.03	Lyα	3.09922	0.00003	21	4	13.22	0.05	
326	4985.58	0.04	0.44	0.03	Lyα	3.10139	0.00022	42	14	13.51	0.19	
327	4986.66	0.04	0.38	0.03	Lyα	3.10200	0.00008	19	13	13.08	0.49	
328	4990.01	0.03	1.36	0.04	Lyα	3.10424	0.00038	58	25	13.32	0.26	β
329					Lyα	3.10494	0.00001	22	2	14.22	0.07	β
330	4994.98	0.01	1.66	0.03	Lyα	3.10890	0.00004	37	3	14.42	0.05	β
331	4996.39	0.01	0.95	0.02	Lyα	3.10994	0.00004	24	2	14.05	0.06	β
332	5001.53	0.08	0.30	0.04	Lyα	3.11426	0.00007	34	7	13.14	0.07	
333	5004.39	0.11	0.18	0.04	Lyα	3.11660	0.00007	21	8	12.91	0.11	
334	5006.08	0.09	0.11	0.03	Lyα	3.11798	0.00010	18	12	12.69	0.16	
335	5008.52	0.05	0.45	0.04	Lyα	3.11993	0.00005	37	6	13.36	0.05	
336	5011.70	0.02	1.76	0.05	Lyα	3.12261	0.00001	37	2	14.42	0.06	β
337	5013.58	0.04	0.14	0.02	Lyα	3.12416	0.00007	16	9	12.86	0.13	
338	5015.29	0.02	1.61	0.04	FeII 2374	1.11195	0.00004	16	3	14.59	0.18	
339					FeII 2374	1.11228	0.00004	18	12	14.75	0.24	
340					FeII 2374	1.11268	0.00092	46	222	14.12	2.92	
341	5017.45	0.02	0.96	0.03	FeII 2374	1.11314	0.00111	44	58	14.07	2.81	
342					FeII 2374	1.11314	0.00004	15	7	14.49	0.20	
343	5018.93	0.05	0.17	0.03	Lyα	3.12840	0.00009	23	13	12.93	0.21	
344	5019.85	0.05	0.09	0.02	Lyα	3.12987	0.00055	67	66	13.19	0.42	
345	5021.70	0.02	0.96	0.04	Lyα	3.13085	0.00002	31	2	13.86	0.04	β
346	5024.67	0.05	0.22	0.03	Lyα	3.13321	0.00004	17	4	13.04	0.06	
347	5027.04	0.03	0.88	0.04	Lyα	3.13522	0.00001	29	2	13.81	0.03	β
348	5028.84	0.02	0.49	0.03	Lyα	3.13678	0.00003	24	3	13.54	0.04	
349	5029.97	0.01	0.87	0.03	Lyα	3.13763	0.00002	17	3	13.97	0.10	
350	5031.02	0.03	0.21	0.03	Lyα	3.13845	0.00003	11	5	13.18	0.07	
351	5033.90	0.02	4.27	0.06	FeII 2382	1.11195	0.00004	16	3	14.59	0.18	
352					FeII 2382	1.11228	0.00004	18	12	14.75	0.24	
353					FeII 2382	1.11269	0.00092	46	222	14.12	2.92	
354					FeII 2382	1.11314	0.00111	44	58	14.07	2.81	
355					FeII 2382	1.11314	0.00003	15	7	14.49	0.20	
356	5037.64	0.06	0.20	0.04	Lyα	3.14390	0.00008	24	9	13.00	0.11	
357	5041.25	0.03	1.51	0.05	Lyα	3.14681	0.00015	42	6	13.84	0.18	β
358					Lyα	3.14718	0.00004	19	4	14.19	0.11	β
359	5047.07	0.05	0.17	0.03	Lyα	3.15188	0.00011	46	14	13.13	0.09	β
360	5048.90	0.03	0.94	0.04	Lyα	3.15323	0.00002	27	2	13.83	0.03	β
361	5053.94	0.06	0.12	0.03	Lyα	3.15745	0.00015	25	18	12.93	0.21	
362	5054.77	0.05	0.22	0.03	Lyα	3.15809	0.00007	11	11	12.97	0.18	
363	5056.98	0.09	0.39	0.05	Lyα	3.16003	0.00011	60	13	13.37	0.07	
364	5059.66	0.06	0.40	0.04	Lyα	3.16194	0.00007	34	8	13.30	0.07	
365	5063.84	0.05	0.22	0.03	Lyα	3.16545	0.00006	22	7	13.10	0.09	
366	5070.87	0.06	0.24	0.04	Lyα	3.17150	0.00013	47	14	13.26	0.11	
367	5072.52	0.03	0.65	0.04	Lyα	3.17280	0.00006	36	8	13.50	0.09	
368	5074.52	0.02	1.76	0.05	Lyα	3.17426	0.00002	43	3	14.28	0.03	β
369	5078.13	0.02	1.11	0.04	Lyα	3.17748	0.00007	55	5	14.04	0.04	β
370	5079.92	0.02	1.72	0.04	Lyα	3.17877	0.00003	32	3	14.32	0.07	β
371	5083.32	0.06	0.60	0.05	Lyα	3.18159	0.00004	37	5	13.53	0.04	
372	5084.97	0.05	0.30	0.04	Lyα	3.18290	0.00004	18	5	13.19	0.07	
373	5086.74	0.08	0.25	0.04	Lyα	3.18439	0.00007	29	8	13.08	0.09	
374	5088.58	0.06	0.51	0.04	Lyα	3.18578	0.00002	18	3	13.46	0.05	
375	5093.26	0.02	3.01	0.05	Lyα	3.18929	0.00079	48	21	14.33	0.88	βγ
376					Lyα	3.18991	0.00015	37	7	14.83	0.29	βγ
377					Lyα	3.19179	0.00104	59	92	13.53	0.80	
378	5096.67	0.02	1.71	0.05	Lyα	3.19257	0.00003	24	4	14.48	0.09	βγ
379	5098.33	0.03	0.72	0.04	Lyα	3.19370	0.00006	31	4	13.73	0.05	β
380	5102.10	0.04	1.77	0.06	Lyα	3.19610	0.00017	46	18	13.41	0.34	β
381					Lyα	3.19713	0.00004	26	5	13.82	0.09	β
382	5104.66	0.04	0.33	0.03	Lyα	3.19825	0.00068	123	86	13.75	0.30	β
383	5107.26	0.02	2.88	0.05	Lyα	3.20053	0.00013	36	6	14.08	0.14	
384					Lyα	3.20154	0.00007	31	4	14.75	0.09	βγ
385	5109.43	0.03	0.19	0.02	Lyα	3.20299	0.00059	73	104	13.55	0.62	
386	5110.73	0.05	0.88	0.05	Lyα	3.20407	0.00007	35	13	13.57	0.40	

TABLE 1—*Continued*

n	λ_{vac} (A)	±	EW	±	ID	*z*	±	*b*	±	log *N*	±	
387	5114.73	0.02	2.04	0.05	Lyα	3.20737	0.00002	36	3	14.66	0.14	βγ
388	5116.97	0.04	1.32	0.06	Lyα	3.20912	0.00002	31	3	14.11	0.06	βγ
389	5124.76	0.11	0.30	0.05	Lyα	3.21560	0.00009	35	10	13.13	0.09	
390	5127.00	0.08	0.16	0.04	Lyα	3.21739	0.00008	14	11	12.84	0.16	
391	5128.12	0.09	0.19	0.04	Lyα	3.21829	0.00012	30	14	13.01	0.14	
392	5130.26	0.06	0.50	0.05	Lyα	3.22009	0.00004	28	4	13.44	0.05	
393	5133.73	0.10	0.30	0.05	Lyα	3.22302	0.00005	33	6	13.18	0.05	
394	5138.66	0.05	3.60	0.12	MLyα	3.22661	0.00026	39	7	15.13	0.35	βγ
395					MLyα	3.22742	0.00019	27	2	15.49	0.26	βγ
396	5141.27	0.02	0.36	0.03	Lyα	3.22917	0.00017	48	36	13.55	0.29	β
397	5142.65	0.03	1.03	0.05	Lyα	3.23037	0.00007	34	5	13.79	0.08	β
398	5144.66	0.07	0.20	0.04	Lyα	3.23197	0.00008	23	10	12.98	0.13	β
399	5146.36	0.02	1.55	0.05	Lyα	3.23336	0.00002	33	3	14.34	0.09	βγ
400	5152.25	0.05	0.27	0.04	Lyα	3.23842	0.00013	33	11	13.42	0.15	β
401	5154.05	0.02	2.11	0.05	Lyα	3.23944	0.00007	23	10	14.21	0.40	β
402					Lyα	3.23994	0.00067	44	27	14.02	0.64	β
403	5157.19	0.06	0.64	0.05	Lyα	3.24233	0.00015	55	17	13.52	0.11	
404	5158.82	0.05	0.36	0.04	Lyα	3.24360	0.00012	31	11	13.22	0.17	
405	5165.70	0.05	0.35	0.04	Lyα	3.24924	0.00004	25	5	13.27	0.05	
406	5167.63	0.03	0.63	0.04	Lyα	3.25085	0.00003	26	3	13.60	0.04	
407	5170.21	0.02	0.56	0.03	Lyα	3.25289	0.00007	14	7	13.41	0.22	β
408	5171.12	0.03	0.57	0.04	Lyα	3.25353	0.00011	32	10	13.72	0.12	β
409	5173.62	0.02	1.52	0.05	Lyα	3.25573	0.00007	36	5	14.11	0.07	β
410	5175.21	0.03	0.73	0.05	Lyα	3.25684	0.00015	44	10	13.80	0.12	β
411	5179.55	0.02	2.33	0.05	Lyα	3.26068	0.00002	42	1	14.67	0.03	βγ
412	5183.32	0.05	1.20	0.06	Lyα	3.26374	0.00005	57	5	13.88	0.03	
413	5185.57	0.04	0.90	0.06	Lyα	3.26563	0.00003	34	4	13.77	0.04	
414	5187.86	0.06	0.37	0.05	Lyα	3.26747	0.00006	24	8	13.30	0.09	
415	5189.80	0.03	1.80	0.07	Lyα	3.26877	0.00046	29	19	13.98	0.62	β
416					Lyα	3.26920	0.00012	16	11	14.05	0.51	
417					Lyα	3.26990	0.00009	17	9	13.31	0.14	
418	5192.96	0.10	0.58	0.08	Lyα	3.27164	0.00008	53	8	13.48	0.05	
419	5195.87	0.19	0.27	0.07	Lyα	3.27426	0.00008	26	9	13.03	0.10	
420	5198.35	0.03	1.44	0.06	Lyα	3.27612	0.00005	29	4	14.20	0.08	βγ
421	5199.65	0.03	0.45	0.05	Lyα	3.27713	0.00007	18	8	13.47	0.11	βγ
422	5200.67	0.05	0.26	0.05	Lyα	3.27804	0.00010	15	13	13.12	0.19	βγ
423	5202.77	0.05	2.82	0.11	Lyα	3.27945	0.00025	44	13	14.44	0.19	βγ
424					Lyα	3.28036	0.00023	35	10	14.24	0.30	βγ
425	5206.32	0.06	1.11	0.09	Lyα	3.28279	0.00003	25	3	14.01	0.06	βγ
426	5218.86	0.07	0.62	0.07	Lyα	3.29298	0.00003	20	3	13.63	0.06	
427	5220.56	0.06	0.79	0.08	Lyα	3.29437	0.00004	35	4	13.69	0.04	
428	5225.11	0.04	1.53	0.07	Lyα	3.29829	0.00007	51	6	14.17	0.05	βγ
429	5227.04	0.06	1.59	0.16	Lyα	3.29967	0.00006	20	5	14.42	0.17	βγ
430	5228.59	0.05	0.34	0.05	Lyα	3.30065	0.00062	64	65	13.57	0.44	βγ
431	5230.13	0.04	1.09	0.06	Lyα	3.30228	0.00004	26	4	13.95	0.07	βγ
432	5235.02	0.06	0.20	0.05	Lyα	3.30631	0.00005	12	7	13.05	0.10	
433	5236.75	0.08	0.24	0.05	Lyα	3.30772	0.00005	15	6	13.12	0.09	β
434	5238.46	0.07	0.59	0.07	Lyα	3.30879	0.00023	26	20	13.15	0.31	β
435					Lyα	3.30941	0.00011	16	16	13.18	0.36	β
436	5239.69	0.03	0.31	0.04	Lyα	3.31015	0.00010	25	17	13.35	0.21	β
437	5240.76	0.05	0.62	0.06	Lyα	3.31103	0.00008	25	7	13.52	0.09	β
438	5244.88	0.11	0.30	0.08	Lyα	3.31439	0.00012	32	13	13.15	0.13	
439	5246.52	0.06	0.19	0.04	Lyα	3.31574	0.00006	14	9	13.18	0.11	
440	5247.61	0.04	0.39	0.05	Lyα	3.31659	0.00006	16	8	13.38	0.10	β
441	5249.31	0.03	1.87	0.07	Lyα	3.31803	0.00003	45	3	14.46	0.04	βγ
442	5253.99	0.04	5.71	0.12	Lyα	3.31953	0.00007	14	8	13.39	0.13	β
443					Lyα	3.32101	0.00006	39	4	15.48	0.08	βγδ
444					Lyα	3.32271	0.00008	49	3	15.61	0.11	βγδ
445	5258.13	0.09	0.32	0.06	Lyα	3.32528	0.00005	21	7	13.23	0.08	
446	5265.58	0.08	0.50	0.08	CIV 1548	2.40099	0.00002	11	3	13.97	0.12	
447	5274.13	0.05	0.36	0.05	CIV 1550	2.40099	0.00002	11	3	13.97	0.12	
448	5275.38	0.07	0.29	0.05	Lyα	3.33951	0.00002	10	3	13.30	0.08	
449	5282.73	0.15	0.92	0.11	Lyα	3.34549	0.00007	66	7	13.66	0.04	
450	5296.08	0.08	0.60	0.09	SiIV 1393	2.79989	0.00002	13	4	13.48	0.07	
451	5297.74	0.07	0.53	0.07	SiIV 1393	2.80124	0.00004	21	5	13.42	0.06	
452	5303.14	0.08	0.19	0.05	Lyα	3.36230	0.00020	73	29	13.36	0.12	
453	5306.71	0.10	0.22	0.05	Lyα	3.36524	0.00008	31	10	13.08	0.09	
454	5309.46	0.03	1.33	0.06	Lyα	3.36752	0.00002	25	1	14.45	0.04	βδ
455	5319.58	0.01	1.38	0.01	Lyα	3.37571	0.00092	23	23	13.90	2.13	

NOTES.—Vertical bars indicate blended features. In a number of cases broad Lyα lines with no apparent local maxima within them require two or sometimes three components to be adequately fitted by Voigt profiles convolved with the instrument profile. In such cases the components listed without a wavelength given apply for the feature with wavelength and equivalent width given above them.

Sometimes severe line blending results in highly uncertain parameter estimates. These cases are marked by an asterisk (*) in place of the parameter error estimates. Greek letters in the last column indicate the higher order Lyman lines used to further constrain the fit to the Lyα listed.

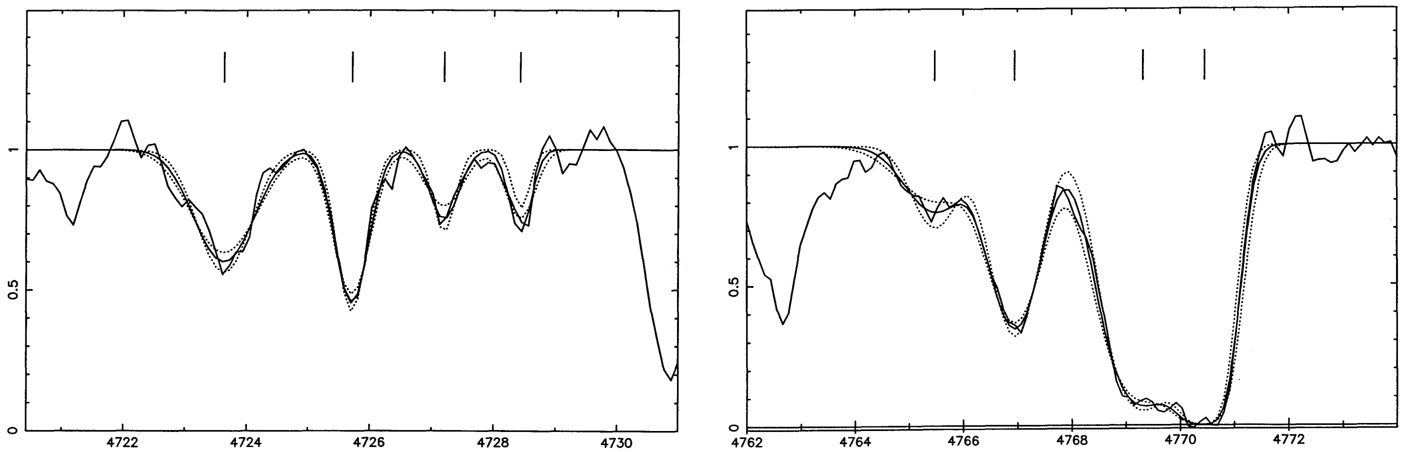

FIG. 3a FIG. 3b

FIG. 3.—Examples of fitted profiles to the Lyα lines. The dotted curves show profiles with the same H I column density and redshift as the best-fit values, but with Doppler parameters 1 σ from the best-fit value. Table 1 gives the parameters for each component.

et al. 1985), it is of value to seek velocity structure in the known systems, as well as to identify any new systems so as to minimize the contamination of the Lyman forest sample by misidentified heavy-element lines.

The procedure used to identify heavy-element systems is similar to that described by Bahcall (1968), which in essence seeks significant excesses of identifications at all possible redshifts within some wavelength tolerance. We use the line list provided by Morton, York, & Jenkins (1988), or subsets containing only the most frequently seen lines. In the present case, a line is listed as a possible member of a heavy-element system if its measured wavelength is within ± 100 mÅ of the predicted position of a metal line at the appropriate redshift. Apart from a requirement that Lyα be present if it would fall in the observed wavelength range, and that multiple transitions from a single ion have equivalent widths consistent (within the errors) with their oscillator strengths, no further constraints were imposed during the automatic search. The lines of heavy-element systems identified in this way are listed in Table 2.

3.1. *The z = 1.11 System*

This system was also found by SBS in their C IV survey and exhibits a series of strong Fe II lines $\lambda\lambda$2260, 2344, 2382. A satisfactory fit seems to require four to five components, but the number is quite uncertain since the lines are very strong and broad. The more reliable components in the edges of the profile yield a b-value in the range 15–18 km s^{-1}. There is also a redshift coincidence with Zn II $\lambda\lambda$2026, 2062 lines at $z = 1.1123$.

If the Zn II identification is correct, then we can estimate the Fe II and Zn II column densities in the $z = 1.1123$ component by simultaneously fitting Voigt profiles to the Fe II $\lambda\lambda$2260, 2344, 2367, 2374, and 2383 and Zn II $\lambda\lambda$2026 and 2062 lines, requiring that the Fe II redshift and b-value match those for Zn II. This condition has little effect on the values obtained but does reduce the resulting error. For this component, we find $z = 1.11229 \pm 0.00002$ and $b = 12 \pm 5$ km s^{-1}, log N(Fe II) = 14.62 ± 0.24 and log N(Zn II) = 12.83 ± 0.11. Since both zinc and iron are likely to be mostly singly ionized, the Zn II/Fe II value of log N(Zn II)/N(Fe II) = -1.8 ± 0.3 can be compared directly with the solar Zn/Fe value of -2.9. This implies an iron depletion of about a factor of 10 in the $z = 1.11$ cloud. In the Galactic interstellar medium, iron is depleted by of order a factor of 100 because of its adherence to grain surface, whereas zinc, which is not refractory, retains its solar value (e.g., de Boer, Jura, & Shull 1987). It is thus possible that some depletion of iron onto dust grains has occurred in the $z = 1.11$ cloud, though it is less than in the Galaxy.

3.2. *The Z = 2.401 System*

This system has a number of lines at $z = 2.401$ including Lyα ($z = 2.4011$, $b = 34$ km s^{-1}, log $N = 14.91$). The most reliable parameters come from the strong C IV doublet ($z = 2.4010$, $b = 11$ km s^{-1}, log $N = 13.97$) and Si IV 1393 ($z = 2.4010$, $b = 13$ km s^{-1}, log $N = 12.86$). A possible C II 1334 at $z = 2.40095$ seems to be very narrow and has rather uncertain parameters.

3.3. *The z = 2.4933 System*

SBS identify a system at $z = 2.4933$, whose Si IV lines should lie in our wavelength range. They erroneously identify λ4899.54 as Si IV 1393 rather than as Si IV 1402 which would be consistent with their redshift value of 2.4928. However there is no corresponding Si IV 1393 visible and so the reality of the λ1402 identification is doubtful.

3.4. *The z = 2.7997, 2.8012 System*

This system exhibits strong Lyα absorption which is well fitted by $z = 2.79958$, $b = 89$ km s^{-1}, log $N = 16.40$. The component structure of Si IV 1393, 1402 ($z = 2.79989$ and 2.80124, $b = 13$ and 21 km s^{-1}, log $N = 13.48$ and 13.42) suggests that Lyα must be double, but a two-component fit to the featureless Lyα line provides no additional constraints. For the $z = 2.80$ two-component there is also a convincing Si II identification ($z = 2.80128$, $b = 19$ km s^{-1}, log $N = 13.05$). Two Si III 1206 components ($z = 2.7997$ and 2.80118) may be real but are blended with further unidentified lines. SBS have also detected C IV 1548, 1550 in this redshift system longward of the QSO Lyα emission line.

3.5. *The z = 3.227 System*

This redshift is derived from fits to Lyα, Lyβ, and Lyγ. We find no heavy-element lines in our spectrum, but on the basis

TABLE 2

HEAVY ELEMENT ABSORPTION SYSTEMS

n	λ_{vac} (A)	ID	z	±	b	±	log N	±
			z = 1.11					
241	4774.58	FeII 2260	1.11195	0.00004	16	3	14.59	0.18
309	4950.86	FeII 2344	.	.	.	.	.	.
338	5014.73	FeII 2374	.	.	.	.	.	.
351	5032.72	FeII 2382	.	.	.	.	.	.
243	4775.34	FeII 2260	1.11228	0.00004	18	12	14.75	0.24
310	4951.64	FeII 2344	.	.	.	.	.	.
352	5033.07	FeII 2382	.	.	.	.	.	.
339	5015.53	FeII 2374	.	.	.	.	.	.
58	4279.78	ZnII 2026	1.11229	0.00002	4	2	13.24	0.57
79	4356.94	ZnII 2062	.	.	.	.	.	.
340	5016.48	FeII 2374	1.11268	0.00092	46	*	14.12	*
245	4776.25	FeII 2260	.	.	.	.	.	.
311	4952.58	FeII 2344	.	.	.	.	.	.
353	5034.02	FeII 2382	.	.	.	.	.	.
246	4777.27	FeII 2260	1.11314	0.00111	44	*	14.07	*
312	4953.64	FeII 2344	.	.	.	.	.	.
341	5017.45	FeII 2374	.	.	.	.	.	.
354	5035.10	FeII 2382	.	.	.	.	.	.
247	4777.28	FeII 2260	1.11314	0.00004	15	7	14.49	0.20
313	4953.65	FeII 2344	.	.	.	.	.	.
342	5017.56	FeII 2374	.	.	.	.	.	.
355	5035.11	FeII 2382	.	.	.	.	.	.
			z = 2.40					
23a	4132.77	MLyα	2.39958	0.00006	64	10	14.25	0.49
23b	4134.66	MLyα	2.40114	0.00004	34	8	14.91	0.05
223	4738.04	SiIV 1393	2.39952	0.00002	32	2	13.48	0.02
137	4538.12	CII 1334	2.40095	0.00003	3	*	13.71	*
446	5265.58	CIV 1548	2.40099	0.00002	11	3	13.97	0.12
447	5274.13	CIV 1550	.	.	.	.	.	.
224	4740.18	SiIV 1393	2.40100	0.00002	13	3	12.86	0.05
			z = 2.80					
170	4619.04	MLyα	2.79958	0.00002	89	4	16.40	0.20
155	4584.33	SiIII 1206	2.79968	0.00005	44	4	13.65	0.06
450	5296.08	SiIV 1393	2.79989	0.00002	13	4	13.48	0.07
156	4586.25	SiIII 1206	2.80118	0.00005	46	5	13.72	0.06
451	5297.74	SiIV 1393	2.80124	0.00004	21	5	13.42	0.06
255	4791.24	SiII 1260	2.80128	0.00003	19	4	13.05	0.05
315	4958.33	SiII 1304	.	.	.	.	.	.
			z = 3.23					
394	5138.16	MLyα	3.22661	0.00026	39	7	15.13	0.35
395	5139.15	MLyα	3.22742	0.00019	27	2	15.49	0.26

NOTES.—Lines denoted as MLyα belong to systems with metal absorption lines. In some cases, severe line blending results in highly uncertain parameter estimates. These cases are marked by an asterisk (*) in place of the parameter error estimates. Additional Lyα components in some of the fitting regions are included in Table 1.

of SBS's detection of C IV at this redshift, the system was omitted from our Lyman forest sample.

4. PROPERTIES OF LYMAN FOREST ABSORPTION SYSTEMS

4.1. *Number-Density Evolution*

Ultimately, we are interested in the evolution of the physical characteristics of the clouds themselves—e.g., the number of clouds of a given size, aspect ratio, ionization fraction, mass, density, and temperature as a function of redshift. Since the equivalent width is one of the more easily measured characteristics of any line, many existing analyses have used equivalent width–limited samples to examine evolutionary characteristics in the forest. Unfortunately, at low resolution it is difficult to separate the contributions of column density and Doppler parameter to the measured equivalent width.

However, with the ever-increasing quality of available Lyman forest data, it is becoming possible to examine column density–limited samples, since the resolution of line profiles allows us to remove the Doppler parameter, column density degeneracy through line-fitting techniques such as we have employed here. Such analysis permits us to estimate the number of clouds associated with each measured line, and to infer the value of the Doppler parameter which provides an upper limit to the cloud temperature.

TABLE 3
REDSHIFT WINDOWS FOR LINE COUNTS

QSO	Redshift Range
0014+813	2.695–3.273
0420−388	2.470–3.070
1100−264	1.840–2.104
2000−330	3.057–3.160
	3.210–3.420
	3.460–3.540
	3.570–3.645

We examine the redshift dependence of the number of Lyman forest clouds by combining the 0014+813 data presented here with those published for 0420−388 (Atwood et al. 1985), PKS 2000−330 (Carswell et al. 1987) and 1100+264 (Carswell et al. 1991). In order to avoid any proximity effects, we restrict our attention only to clouds whose redshift places them sufficiently far from the QSO that its radiation does not dominate their environment (except for 0420−338, where a Lyman limit system at $z = 3.08$ removes the ionizing flux from the QSO as seen by systems at lower redshifts). So that we may compare our results directly to those of Lu, Wolfe, & Turnshek (1991), we adopt this distance to be 8 Mpc. The redshift ranges covered by the data for each QSO are summarized in Table 3.

The number-redshift relation is conventionally parameterized as a power law of the form $dN/dz \propto (1 + z)^{\gamma}$, and it is instructive to investigate the sensitivity of γ to various conditions placed on the same input data. Table 4 summarizes the values of γ derived using three different line selection criteria. Cases A and B set line selection thresholds based on the inferred cloud column density rather than the measured line equivalent width. The column density threshold in case A was chosen so as to select as large a complete sample as possible; that in case B was chosen so that the rest equivalent width at $b = 33$ km s^{-1} is 360 mÅ, the equivalent width threshold adopted by Lu et al. (1991). Although the evidence for positive evolution in the number of clouds with redshift is clear, there is no evidence in our data for any difference in evolution between high- and low-column density clouds.

In case C we restrict our sample to those lines, whether single or blended, whose integrated rest equivalent width exceeds 360 mÅ. The number-density evolution of this sample can then be compared directly to that inferred by Lu et al. (1991), who adopted the same limit for a complication of 952 lines from 38 QSOs. Even though the resolution of our data is considerably higher than that of Lu et al., Parnell & Carswell (1988) have shown γ to be relatively insensitive to resolution, so that this comparison may be a valid one.

We infer $\gamma = 1.68 \pm 0.80$ from our equivalent width–limited sample while Lu et al. infer $\gamma = 2.75 \pm 0.29$ from theirs. Although the difference between these values is within the 1 σ error bars of the separate determinations, it is interesting to note that Lu et al. present evidence for a break in the power law at $z = 2.32$ and fit a double power law with $\gamma = 2.28$ above and 4.21 below that redshift. Our sample contains only five lines with $W_{rest} > 360$ mÅ below this redshift, so we find good agreement between Lu et al.'s high redshift result and ours but are unable to comment on the presence of a steepening of the power law at lower redshifts. However, we note that such an effect is likely to be in conflict with the result of Morris et al. (1991) who find a significant excess of lines near zero redshift compared to the number predicted by extrapolating from high redshift; a steeper power law will lead to an even smaller predicted number of clouds.

TABLE 4
POWER-LAW EXPONENTS FOR THREE LINE SELECTION CRITERIA

Case	Selection Criterion	Number of Lines	γ
A	$\log N > 13.75$	301	2.08 ± 0.53
B	$\log N > 14.27$	120	1.59 ± 0.82
C	$W_{rest} > 360$ mÅ	127	1.68 ± 0.80

4.2. *The Column Density and Doppler-Width Distributions*

In order to study the column density distribution of the Lyman forest clouds toward 0014+813, proper account must be taken of the selection effects which arise in identifying lines in the observational data. Line-finding routines tend to impose a noise-dependent cut off at low equivalent widths, such that in regions of lower S/N the weaker lines will be missing. To examine the N(H I) distribution, we have selected only those lines above the 4 σ level with respect to the continuum in order to minimize the number of spurious features. Under this restriction, a line with $b \lesssim 80$ km s^{-1} is detectable for $\log N(\text{H I}) \gtrsim 13.3$. Since there are few lines with larger inferred b-values (five of 295), this H I column density provides a reasonable completeness limit.

The "proximity effect–free" sample for which $\log N \gtrsim 13.3$ contains 166 lines in a redshift interval $2.695 \leq z \leq 3.273$ at a mean redshift of 2.996. The distribution of the number of systems $\mathcal{N}$ per unit redshift versus column density is well represented by a power law, $d\mathcal{N}/dN \propto N^{-\beta}$, $\beta = 1.74 \pm 0.06$ (Fig. 4). A K-S test gives the probability for a power-law representation as 0.51. The mean b-value for the sample is 36 km s^{-1} with a first moment about the mean of 16 km s^{-1}; the median value is 33 km s^{-1}.

The full $\log N \gtrsim 13.3$ sample (ignoring proximity effects) contains 189 lines in the redshift interval $2.695 \leq z \leq 3.376$ at a mean redshift of $z = 3.03$. The inferred value of β is 1.72 ± 0.05, and the mean, median, and first moment of b are unchanged from the proximity effect–free sample. Because the two samples are indistinguishable, we use the full sample in what follows.

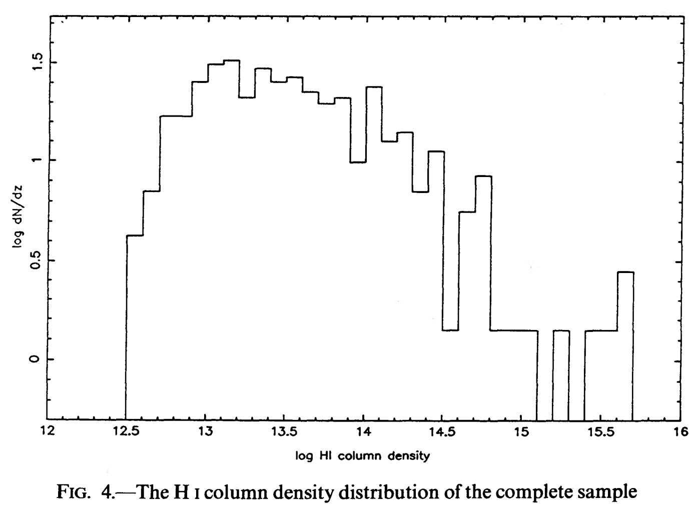

FIG. 4.—The H I column density distribution of the complete sample

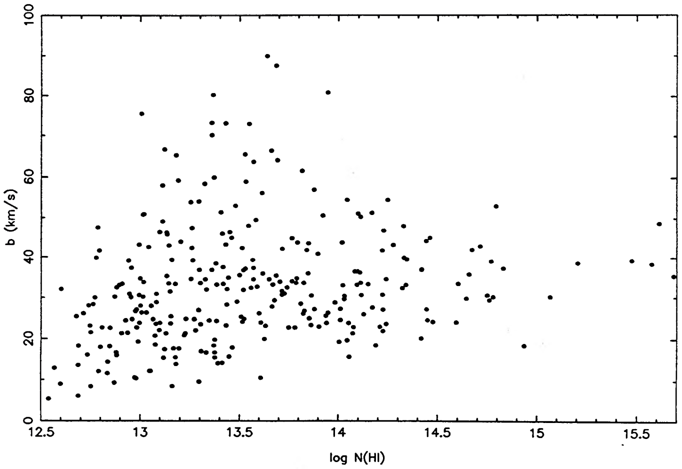

FIG. 5.—Doppler parameter b vs. log N (H I) for the full line sample

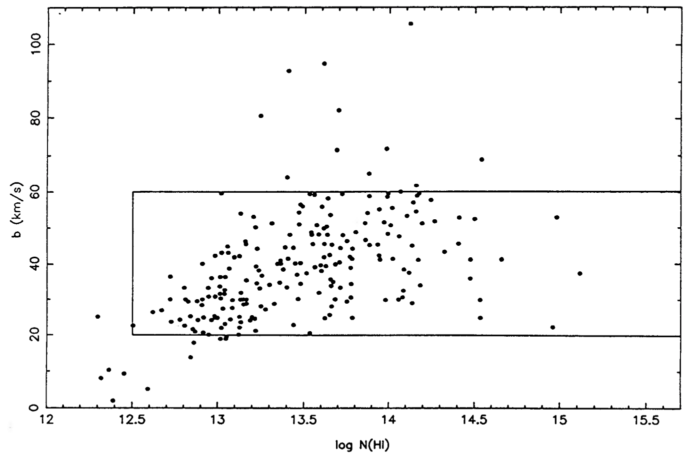

FIG. 6.—The b vs. log N for the fitted results for a simulated line sample. (Input parameters were confined to those within the rectangular box.)

4.3. *Doppler-Width, Column Density Relationships*

For the sample described in the previous section, a correlation coefficient of 0.101 is found between b and log N(H I) which has a probability of 0.19 of occurring by chance for uncorrelated distributions in the variables. There is thus no evidence for any significant b–log N correlation for the log $N \gtrsim 13.3$ subsample.

However, when we consider all 295 lines we have identified as Lyα arising in Lyman forest systems, Figure 5 illustrates that those with log $N \geq 13.75$ appear to have fewer lines with $b \leq 20$ km s^{-1} (six of 98) than do those with log $N < 13.75$ (41 of 198). Furthermore, there is a positive correlation between b and log N for column densities below $\simeq 13.75$ dex which is absent for higher column densities. To investigate this effect further, we split the sample into two subsamples: (*a*) the 197 lines with log N(H I) ≤ 13.75, and (*b*) the 98 with log N(H I) > 13.75. A b–log N correlation coefficient of 0.014 and a random probability of 89% is obtained for the higher column density subsample, suggesting that, like the complete sample, it exhibits no significant b–log N correlation. However, the lower column density subsample has a correlation coefficient of 0.35, with chance probability for uncorrelated data $< 10^{-6}$.

In fact, as we now show, these apparent correlations of Doppler parameter and column density can be accounted for *entirely* by biases in the line-finding and fitting procedures applied to a given line sample. To demonstrate this, we have chosen to simulate a spectrum containing Lyα lines with a simple, known distribution of Doppler parameters and column densities and to search for and fit lines in the usual manner. The spectrum was generated from a sample of lines, which, for simplicity, occupy a horizontal bar in b–log N parameter space, being confined to the intervals $20 < b < 60$ km s^{-1}, $12.5 < \log N < 15.7$. The lines were distributed randomly in redshift and Doppler parameter with the same number density as the real 0014+813 spectrum (although covering a slightly reduced redshift range so that the total number of lines observed is smaller than in 0014+813). The column density distribution obeyed the empirically determined $\propto N_{\rm col}^{-1.74}$ power law. The simulated spectrum was convolved with the (Gaussian) instrumental profile, and noise was introduced to mimic the resolution and S/N of the observed spectrum.

Qualitatively, Figure 6, which presents the b–log N(H I) plot resulting from Voigt profile fits to the spectrum that arises from this rather featureless sample, reproduces the basic features of the real data surprisingly well:

1. A number of "runaways" with high Doppler parameters arise from unresolved blends.

2. Another group of lines appears beyond the low b–low log N corner of the box-shaped input sample, implying that some fits result in unrealistically narrow weak lines. These lines undoubtedly arise from S/N effects.

3. There is a triangular zone, bordered by log $N = 12.5$, $b = 60$ km s^{-1} and the diagonal line joining log $N = 13.2$, $b = 60$ km s^{-1} and log $N = 12.5$, $b = 20$ km s^{-1}, in which lines have almost completely disappeared, despite their having been a high line number density in the input sample to this region. This zone of avoidance results because the line detection threshold is set by the S/N over the entire line profile, which at any given equivalent width is lower for broader, shallower lines, and thus these will be preferentially rejected.

4. The region with log $N \gtrsim 13.5$ and $b \lesssim 25$ km s^{-1} appears to have been systematically depopulated as well. This seems likely to arise from the fact that lines produced by clouds with these column densities have a better determined b because of their position on the curve of growth. This results in a reduced vertical scatter in Figure 6 compared to lower column densities, with most points (apart from the "runaways") confined to the initial condition box. The depopulation of *lower b* systems within the box then arises from an apparent systematic broadening of lines due to blending. Low-b lines may be more sensitive to blending than lines which have a truly higher b since in cases where a narrow log $N \leq 13.5$ line is blended with a broader log $N \geq 13.5$ one, χ^2 (and hence the parameter error estimate) is dominated by the broad component.

These selection effects combine to imprint a highly significant correlation of 0.39, similar to that observed in the real data, on the uncorrelated parent line population, and suggest that the observed correlation seen in Figure 5 results entirely from these effects. (We note that in spite of these changes, the mean Doppler parameter of the sample is not significantly modified—we obtained $\bar{b} = 39.6$ km s^{-1} for the simulated sample compared to an unblended mean of 40.)

While the above analysis was undertaken for a resolution of ~ 23 km s^{-1} to understand selection effects in the 0014+813 data, similar work at resolution ~ 8 km s^{-1} by Webb & Carswell (1991) yields the same general results.

On the basis of the results from the simulation, we suggest there is no evidence for a difference in the Doppler parameters for high- and low-column density clouds. If there is a true intrinsic difference, it will be difficult to separate from the systematic biases described above.

4.4. *Does the Doppler Parameter Measure Thermal Motions?*

The controversy aroused by the low Doppler parameters (<10 km s^{-1}) reported by Pettini et al. (1990) and the equanimity with which we present Doppler parameters estimates in excess of 60 km s^{-1}, point to the important astrophysical issue behind such measurements. So long as Doppler parameters were found to be of the order of 20 km s^{-1}, their interpretation as thermal motions in clouds seemed consistent with models of galaxy-sized, mostly ionized clouds heated by the integrated intergalactic UV radiation field. However, neither the low b-values proposed by Pettini et al. nor those much in excess of 20 km s^{-1} are consistent with this "standard" model for the hydrogen-only clouds, although in the former case, Duncan, Vishniac, Ostriker (1991) have shown that inclusion of adiabatic cooling as the confining pressure drops may substantially lower the cloud temperature.

While our resolution is not as high as those obtained in a spectrum of 1100−264 by Carswell et al. (1991), and Pettini et al. (1990) in their spectrum of 2206−199, the equivalent width detection limits are similar. Thus we are able to make a comparison between the relative frequencies of narrow lines in each of the objects, provided only that the threshold dividing the low- and high-Doppler parameter subsamples is well above that corresponding to the poorest spectral resolution. It is thus difficult to comment on the number of very narrow systems toward 0014+813 (e.g., with Doppler parameters $\sim$10 km s^{-1}) because our spectral resolution is too poor to measure these reliably. However, choosing a threshold of 20 km s^{-1}, about 12% of the putative Lyα systems in our sample have Doppler parameters less than this value. This value is in good agreement with the sight line toward 1100−264 (Carswell et al.) where about 18% of the lines which are not identified with heavy elements may have Doppler parameters less than 20 km s^{-1}. The comparison with Pettini et al. is more difficult because the lines they chose to fit were those which were both unsaturated and unblended so there will be some additional biases in their sample (see § 4.3 and Webb & Carswell 1991). If we ignore this problem, their profile fits yield 63% for the narrow-line fraction.

It is possible to reconcile high measured b-values with the standard model by proposing that any observed line whose inferred b-value substantially exceeds 20 km s^{-1} results from an unresolved blend in the data. In order to investigate the consequences of such an interpretation, we have adopted $b = 20$ km s^{-1} for all components, thus leaving only column density and redshift as free parameters, and have reapplied our fitting procedure to all Lyα lines in Table 1.

A satisfactory fit can always be obtained by inserting enough sufficiently narrow components into a given observed feature. However, if the fit is to be optimized by minimizing its reduced χ^2, fixing the Doppler parameter at a preconceived value that is lower than the "true," a priori unknown, value may force overfitting of the line to compensate for the incorrect assumed Doppler parameter. In other words, it is difficult to determine whether a bad χ^2 indicates too few fit components or merely reflects an unsuitable line width of one or more of them.

In order to proceed in a consistent manner, we adopted the procedure of inserting additional components until the probability for the achieved reduced χ^2 exceeded 1%. This procedure results in an average reduced $\chi^2 = 1.24 \pm 0.05$, well above that usually obtained for fits with free Doppler parameters at the same probability threshold. To achieve even this result 54% more components were needed to fit the ensemble of lines.

The availability of Lyβ for a subset of the Lyα lines should provide a further constraint on the fitting parameters. Such Lyα + Lyβ fits invariably required about twice as many components as did the corresponding Lyα fit alone. This occurs because Lyα lines are more saturated than the corresponding Lyβ lines, and what may appear to be a satisfactory fit by, for example, two suitably spaced components to a mildly saturated Lyα tends to be clearly inadequate for its corresponding Lyβ.

However, only a minority of systems exhibit unblended Lyβ lines so that this additional constraint cannot be applied to the entire Lyα line set. Its application to only part of the set would inevitably lead to a bias whereby Lyα + Lyβ systems would appear to have more components than Lyα only systems. In order to avoid such a bias, Lyβ was not used to constrain the Lyα fits.

The two-point correlation function (TPCF) of the resulting sample of 453 components with $b = 20$ km s^{-1} is shown in Figure 7 and clearly displays an increased amplitude on small scales ($\Delta v < 100$ km s^{-1}), because several narrow components are needed to reconstruct the observed line. There is an excursion of 4.3 σ which peaks at about 45 km s^{-1}, and the clustering appears to extend out somewhat further. It is clear that because of the effects mentioned above the actual number of components per blend is likely to be significantly higher, so that the clustering amplitude shown in Figure 7 must be seen as a strict lower limit if $b = 20$ km s^{-1}.

Thus, high inferred b-values can be reconciled with standard "warm" cloud models if they are really unresolved blends of $b = 20$ km s^{-1} lines, although such an assumption produces a strong TPCF hitherto associated with only the metal-containing systems, though at much smaller spacings. Alternatively, the Doppler parameter could reflect the existence of nonthermal bulk motions. In either case, very high resolution and S/N observations of such systems should show incipient structure, asymmetries, or other departures from Voigt profiles.

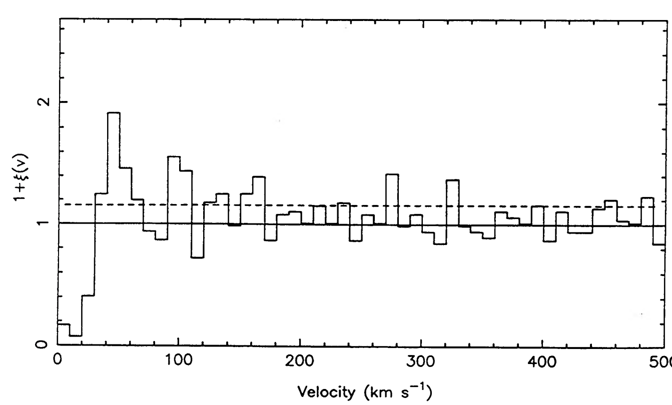

FIG. 7.—The two-point correlation function for 453 lines with fixed Doppler parameter $b = 20$ km s^{-1}. The bins are 10 km s^{-1} wide.

4.5. *Voids in the Lyman Forest*

There have been a number of attempts to search for voids in the Lyman forest, and conflicting conclusions have recently been put forth for their existence. In particular, Crotts (1987, 1989) has presented evidence for possible voids in the forest toward Q0420−388, while Carswell & Rees (1987) find no such evidence. Bechtold (1990) has shown that there are weak Lyα lines in the possible void toward Q0420−388, and Duncan, Ostriker, & Bajtlik (1989) have found little evidence for voids. Recently, however, Dobrzycki & Bechtold (1991) have found a void in the Lyα line distribution toward Q0302−003.

The extended wavelength coverage in 0014+813 invites a search for large-scale gaps or regions of low line density in the forest, and in order to do so we performed the following simple statistical test. The distribution of maximum intervals expected if Lyman forest clouds are randomly distributed along the line of sight [subject to an underlying trend of $dn/dz \propto (1 + z)^2$] was derived using a Monte Carlo simulation of a large number of spectra. The line number density and redshift range used was chosen to match that of 0014+813 over the redshift interval $2.6956 < z < 3.3362$. The lower limit corresponds to the Lyβ emission line and the upper limit to 3000 km s^{-1} below the Lyα emission line, to avoid environmental effects in the QSO vicinity. In this region, we count 187 Lyα absorption lines with log N greater than our adopted completeness level of 13.3 (including those with associated heavy element absorption).

We generated 10,000 line lists, the number of lines in each being selected at random from a Poisson distribution with a mean of 187. Line blending was ignored since the spectral resolution is high and is unlikely to introduce any significant systematic effects on large scales. In Figure 8 we plot the probability distribution of maximum intervals containing 0, 1, 2, and 3 lines. The four arrows above the curves illustrate the observed values for 0014+813. In each case the observed maximum interval lies close to the mean of the simulated distribution, and this simple test yields no obvious evidence for large scale voids or regions of low absorption line number density.

Out of curiosity, we applied the simple method described above to the spectrum of 0420−388, in which Crotts (1987) has reported the existence of a statistically significant void, measuring as before the maximum intervals in the data containing 0, 1, 2, and 3 lines. Once again, we restricted our analysis to the redshift range beginning at Lyβ emission and ending 3000 km s^{-1} below Lyα. For 0420−388, this corresponds to $2.4762 \leq z \leq 3.0788$. The data quality is somewhat lower than that for 0014+813, and only lines above a completeness level of log $N = 13.75$ were included (100 lines in the adopted redshift window). Using probability distributions analogous to those for 0014+813 in Figure 8, we find that the probabilities of the 0, 1, 2, and 3 line maximum gaps arising by chance are 9.3, 6.3, 15.9, and 0.81%.

The 0 line maximum interval corresponds to Crotts's gap (although since we adopt a detection threshold of log $N = 13.75$ our gap extends over the slightly larger range $2.59775 < z < 2.55556$). We conclude therefore that this feature is not statistically significant. However, the spectral region around this feature does appear to have a meager forest and a much more significant effect is seen if we allow the maximum interval to contain three lines. Thus while we disagree with Crotts's specific claim, there is a significant line deficit over the range $2.65259 < z < 2.55556$, corresponding to a scale length of $\sim$8100 km s^{-1} or approximately 24 Mpc (adopting $H_0 = 50$ km s^{-1} Mpc^{-1} and $q_0 = \frac{1}{2}$).

If such an apparent void results not from a real dearth of matter, but from increased local ionization in its vicinity, such a source should be detectable. Indeed, the scale over which the line deficit extends is so large that it seems extremely unlikely that a single ionizing source could have escaped detection. To illustrate the point, we compute the number of lines in this interval expected on the basis of a $q_0 = \frac{1}{2}$ universe, a uniform background radiation of 1.0×10^{-21} ergs s^{-1} Hz^{-1} cm^{-1}, and an "un-ionized" initial mean number of clouds with column densities log $N \geq 13.75$ of 12.7 (derived using $\gamma = 1.987$ and a

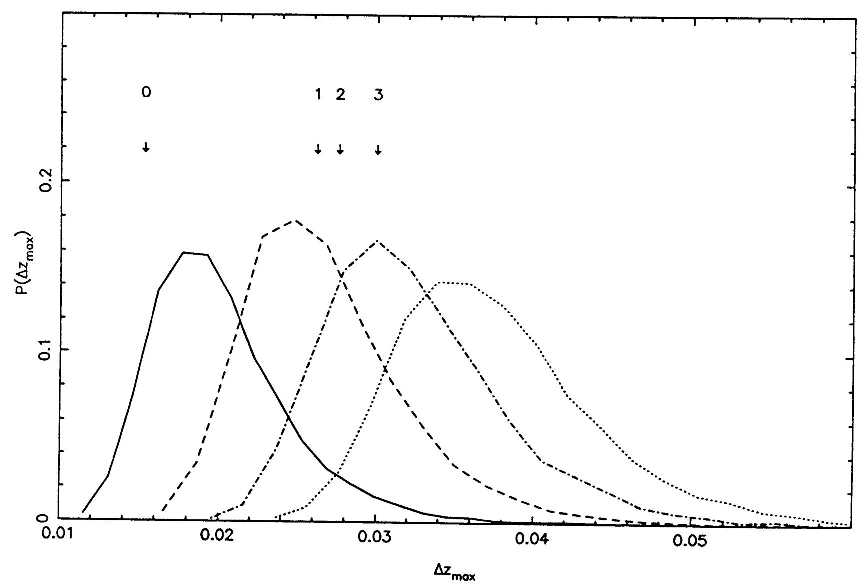

FIG. 8.—The distribution of maximum redshift intervals. The four curves are derived from Monte Carlo runs of randomly distributed absorption lines and from right to left correspond to intervals containing 0, 1, 2, and 3 lines. The four arrows illustrate the observed values toward 0014+813.

line number density at $z = 0$ of 10.3—work to be presented elsewhere). If we assume the offending ionization source lies optimally *on* the line of sight, then in order to reduce the observed number of lines to 3, we require a source with a flux at its Lyman limit of $f_\nu \approx 2.7 \times 10^{-26}$ ergs s^{-1} Hz^{-1} cm^{-2}, which allowing for *k*-corrections (Evans & Hart 1977) and using the empirical expression given by Tyler (1987) translates to a fairly conspicuous $m_v = 14.8$.

On this basis it appears that the observed line deficit is either a statistical fluke or is the result of some other physical mechanism banishing Lyα clouds from the region. QSO variability might offer at least a partial explanation so it would seem worthwhile to make a detailed search of the regions at $z \sim 2.6$ close to the line of sight to 0420−388. Christiani & Shaver (1987) report the discovery of a very faint object, Q0420−388B ($m_v = 20.8$), lying about 1.7 Mpc from the line of sight at $z = 2.40$, so this is unlikely to produce the low observed cloud number density.

Another possibility is the presence of a nearby supercluster at $z \approx 2.6$, perhaps located in a region of high ambient pressure, unfavorable to the formation or survival of Lyα clouds. Christiani & Shaver (1988) detect an absorption system at $z = 2.403$, presumably associated with 0420−388B, in the spectrum of its higher redshift neighbor. As they point out, the redshift difference between the foreground QSO and the associated absorption suggest the presence of a cluster. It would be valuable to make a detailed, high S/N study of 0420−388 longward of the Lyα emission line to search for peculiarities in the number density of C(IV) doublets which might be associated with such a structure.

4.6. *Clustering in the Lyman Forest*

In order to search for possible clustering of Lyman forest clouds, we present in Figure 9 the TPCF for all 295 Lyα lines. The dashed line marks the standard deviation expected from a Poissonian distribution of line-pair velocity separations, and the plot is normalized to a value of $\xi = 0$ for the range from 1050 to 3050 km s^{-1}. There is no convincing evidence for clustering on any scale. Chernomordik (1988) noted the double appearance of selected features toward 0014+813 and suggested a possible interpretation of some Lyα clouds as shocked shells in the intergalactic medium. However, the absence of any clear signal on scales ~100 km s^{-1} suggests this is not a general feature.

Although there is no evidence for general cloud clustering, one unusual aspect of the low-*b* clouds seems to survive selec-

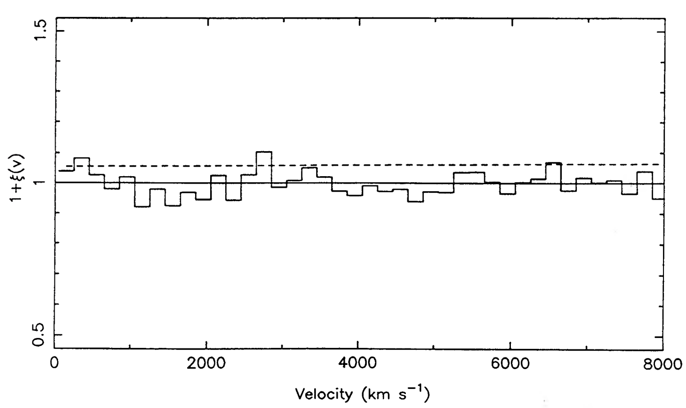

FIG. 9.—The two-point correlation function of the full sample

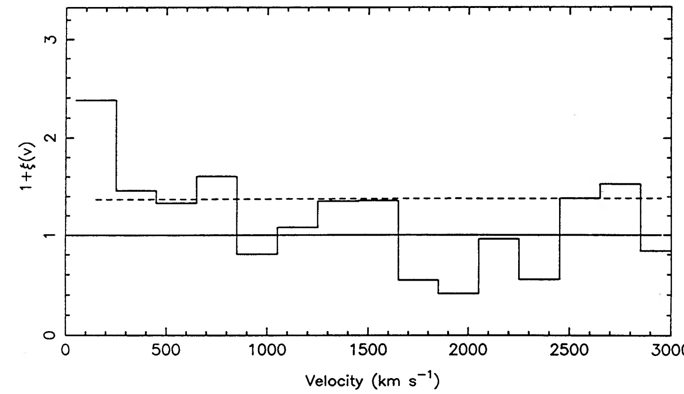

FIG. 10.—The two-point correlation function of the narrow-line sample

tion biases: an examination of the redshifts of such clouds suggests that they tend to occur in groups, mostly separated by less than 3 Å from their neighbors. To check whether this is a general characteristic of the whole sample or a special feature of the narrow lines, we compare the TPCF of the 48 line subsample having $b \leq 20$ km s^{-1} with the remaining 247 lines having $b > 20$ km s^{-1}.

In Figure 10 the TPCF of the narrow-line sample is plotted in 200 km s^{-1} bins over a range from 50 to 3050 km s^{-1}. There is a 2.6 σ excess on scales to about 250 km s^{-1} and some marginal evidence that there is clustering to scales of order 1000 km s^{-1}. This contrasts with the TPCF shown in Figure 9 for all 295 systems measured where there is no evidence for clustering on any scale.

It remains possible that the narrow-line population is distributed uniformly, and evidence for clustering is introduced spuriously by the relative ease of detecting narrow lines in regions in which stronger broad lines are absent. To test whether this effect could cause artificial clustering on the scale in question, we replaced the lines with $b \leq 20$ km s^{-1} in the full observed sample by a population of 160 lines with the same values of *b* and *N* but randomly distributed in wavelength with number density 0.19 Å^{-1} over the whole spectrum. This number density was adopted in order to produce ≃50 detectable narrow lines.

From the full list we then generated an artificial spectrum in which the lines were fitted automatically by Lyα Voigt profiles. The TPCF for the resulting sample of the 60 detected lines with $b \leq 20$ km s^{-1} is shown in Figure 11 and displays no evidence of significant clustering. The artificial spectrum differs from the real data in that we assumed constant instrumental resolution and S/N and a uniform number density of narrow lines with wavelength. Nonetheless, it seems likely that had the correlation seen in the real data (Fig. 10) been caused by a bias favoring the detection of weak lines in regions bereft of strong, broad lines, then that correlation should have appeared clearly in the artificial data (Fig. 11).

Closer scrutiny reveals that the positive signal in the narrow-line TPCF is dominated by nine lines in the range $2.808 < z < 2.835$, five of which are within a 500 km s^{-1} window. Since the clustered component is easily identifiable, and the velocity splittings are comparable to those typically found in heavy-element systems, we examine the Lyα lines at $z \sim 2.8$ in detail to see if they might be heavy element lines which we failed to identify. Most possibilities are excluded by

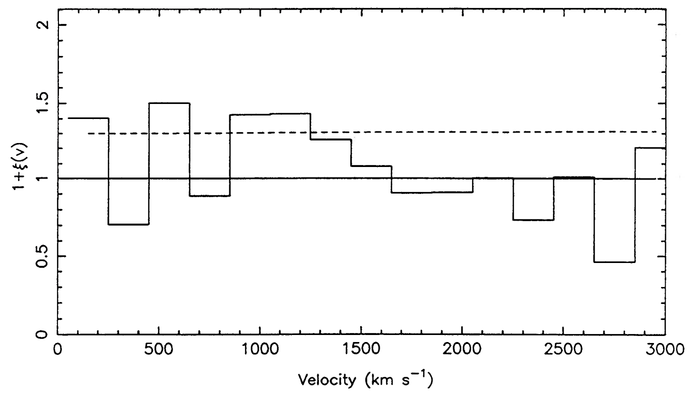

FIG. 11.—The two-point correlation function of a simulation with 60 narrow lines.

the absence of other lines, either from the same ion (e.g., Mg II, Fe II), or from other abundant ions (particularly Lyα) at the same redshifts.

However, we cannot rule out an identification with some solitary heavy element line such as Al II 1670. If this were the correct identification, other metal lines at the same redshift that would fall within our observed wavelength range would be too weak to be detected.

An alternative possibility is that the narrow lines clustered at $z \sim 2.8$ are Lyα lines of low column density, heavy-element systems, where heavy-element cooling would reduce the thermal width of the lines produced in the clouds. Such an explanation seems rather ad hoc, for while there is some evidence that moderate-to-low column density systems may in fact contain metals (Lu 1991; Blades 1988), the metal abundance is probably too low to contribute significantly to the cooling. Evidently, 0014+813 invites further study at higher resolution and S/N.

5. CONCLUSIONS

We summarize our principal results as follows:

1. The observations of 0014+813 reported here are solely of the Lyman forest region, so little new information has been obtained on heavy-element systems. One case is worthy of note: a heavy element system at $z = 1.11$ has a component in which it appears that the Zn/Fe ratio is significantly higher than the solar value. If the identification of the two Zn II lines is correct, this suggests that the iron is depleted, presumably onto dust grains.

The picture we present for the bulk of the Lyα lines is similar to that which has been found in earlier QSO studies at $\simeq 20$ km s^{-1} resolution where all the lines observed have been analyzed:

2. Our data combined with those at similar resolution and S/N for three other QSOs suggest that the number of Lyman forest clouds per unit redshift is well represented by a power law in $(1 + z)$ with an index of 2.1, though the value of the index is sensitive to the redshift range of the available line sample, and the particular set of criteria used to define the sample.

3. The H I column density distribution for clouds with $2.7 < z < 3.4$ is well described by a power law with numbers per unit column density $\propto N^{-1.74\pm0.06}$ for log N(H I) > 13.3. This agrees well with determinations in other objects at other redshifts: $N^{-1.7\pm0.1}$ for log $N > 13$ and $1.84 < z < 2.15$ toward Q1100−264, Carswell et al. (1991); $N^{-1.89\pm0.14}$ for log $N > 14.0$ and $2.47 < z < 3.08$ toward Q0420−388, Atwood et al. (1985); $N^{-1.76}$ for log $N > 13.75$ and incomplete coverage in the range $3.3 < z < 3.8$ toward PKS 2000−330, Carswell et al. (1987). Taken together, these results suggest that the column density distribution function maintains its shape over the redshift range $2 \lesssim z \lesssim 3.5$ for log $N \gtrsim 13.5$.

4. Doppler parameters have a range of values, with a median of about 35 km s^{-1}. For those systems with log $N > 13.3$, where few of the high b-value lines will be missed because of selection effects, the median value of b is 33 km s^{-1}. This is similar to the values found toward Q1100−264 (34 km s^{-1} for log $N > 13$), Q0420−388 (35 km s^{-1} for log $N > 13.75$), and PKS 2000−3300 (37 km s^{-1} log $N > 14$).

5. The fraction of low Doppler parameter ($b < 20$ km s^{-1}) lines seen in 0014+813 is ~12%. This is comparable with the fraction found in 1100−264 (Carswell et al. 1991), but inconsistent with the 63% found from the analysis of 2206−199 by Pettini et al. (1990). The spectral resolution in the data described here is not high enough to investigate the existence or otherwise of very narrow $b < 10$ km s^{-1} Lyα lines.

6. There is no convincing evidence for a correlation between b-value and H I column density for the systems with log $N >$ 13.3. There is an apparent excess of weak narrow lines corresponding to lower H I column densities, but this excess is likely caused by a combination of our missing any broad weak lines and/or to increased errors at low equivalent widths.

7. A search for voids, regions along the line of sight to 0014+813 where the line number density is significantly lower than the mean, proved negative. However, the same technique applied to 0420−388 revealed a region of approximately 24 Mpc where the line density differs from the expected value at a significant level of around 99%. This low-density zone is unlikely to be caused by a nearby ionizing source.

8. The Lyα lines as a whole show no clustering in the redshift range $2.7 < z < 3.4$, but if we consider only the narrow lines which have not been identified with heavy elements then there is significant clustering on scales of ≤ 250 km s^{-1} with some evidence that the effect extends out to ~1000 km s^{-1}. The peak in the two-point correlation function which yields this result is due almost entirely to a group of nine lines identified as Lyα with $z \sim 2.8$. It is possible that these are unidentified heavy element lines, but we have been unable to find any evidence to support such an identification.

We are grateful to the Kitt Peak mountain staff for assistance with the observations, and the U.K. Science and Engineering Research Council for provision, through STARLINK, for the computing facilities used to perform much of the data analysis. F. H. C. gratefully acknowledges the hospitality of the Institute of Astronomy and the support of a Royal Society Guest Research Fellowship. C. B. F. acknowledges support from NSF grant AST 90-01181.

REFERENCES

Atwood, B., Baldwin, J. A., & Carswell, R. F. 1985, ApJ, 292, 58
Bahcall, J. N. 1968, ApJ, 153, 679
Bechtold, J. 1990, in Evolution of the Universe of Galaxies, ed. R. G. Kron (ASP Conf. Ser., 10), 234
Blades, J. C. 1988, in QSO Absorption Lines: Probing the Universe, ed. J. C. Blades et al. (Cambridge: Cambridge Univ. Press), 147
Carswell, R. F., Lanzetta, K. M., Parnell, H. C., & Webb, J. K. 1991, ApJ, 371, 36

Carswell, R. F., Morton, D. C., Smith, M. G., Stockton, A. N., Turnshek, D. A., & Weymann, R. J. 1984, ApJ, 278, 486
Carswell, R. F., & Rees, M. J. 1987, MNRAS, 224, 13P
Carswell, R. F., Webb, J. K., Baldwin, J. A., & Atwood, B. 1987, ApJ, 319, 709
Chaffee, F. H., Foltz, C. B., Bechtold, J., & Weymann, R. J. 1986, ApJ, 301, 116
Chaffee, F. H., Foltz, C. B., Röser, H. J., Weymann, R. J., & Latham, D. W. 1985, 292, 362
Chernomordik, V. V. 1988, Soviet Astron., 32(1), 6
Cristiani, S., & Shaver, P. A. 1988, in "QSO Absorption Lines: Probing the Universe (poster paper collection)," STScI preprint
Crotts, A. P. S. 1987, MNRAS, 228, 41P
———. 1989, ApJ, 336, 550
de Boer, K. S., Jura, M. A., & Shull, J. M. 1987, in Exploring the Universe with the *IUE* Satellite, ed. Y. Kondo (Dordrecht: Reidel), 485
Dobrzycki, A., & Bechtold, J. 1991, ApJ, 377, L69
Duncan, R. C., Ostriker, J. P., & Bajtlik, S. 1989, ApJ, 345, 39
Duncan, R. C., Vishniac, E. T., & Ostriker, J. P. 1991, ApJ, 368, L1
Evans, A., & Hart, D. 1977, A&A, 263, 79
Horne, K. 1986, PASP, 98, 609
Khare, P., York, D. G., & Green, R. F. 1989, ApJ, 347, 627
Kühr, H., Liebert, J. W., Strittmatter, P. A., Schmidt, G. D., & Mackay, C. D. 1983, ApJ, 275, L33
Lu, L. 1991, ApJ, 379, 99
Lu, L., Wolfe, A. M., & Turnshek, D. A. 1991, ApJ, 367, 19
Morris, S. L., Weymann, R. J., Savage, B. D., & Gilliland, R. L. 1991, ApJ, 377, L1
Morton, D. C., York, D. G., & Jenkins, E. B. 1988, ApJS, 68, 449
Parnell, H. C., & Carswell, R. F. 1988, MNRAS, 230, 491
Pettini, M., Hunstead, R. W., Smith, L., & Mar, D. P. 1990, MNRAS, 246, 545
Sargent, W. L. W., Boksenberg, A., & Steidel, C. C. 1988, ApJS, 68, 539 (SBS)
Sargent, W. L. W., Steidel, C. C., & Boksenberg, A. 1989, ApJS, 69, 703
Tytler, D. 1987, ApJ, 321, 69
Webb, J. K., & Carswell, R. F. 1991, in Proc. ESO Mini-Workshop on Quasar Absorption Lines (ESO Report 19), in press
Wolfe, A. M. 1991, in Proc. ESO Mini-Workshop on Quasar Absorption Lines (ESO Report 19), in press
Young, P. J., Sargent, W. L. W., Boksenberg, A., Carswell, R. F., & Whelan, A. J. 1979, ApJ, 229, 891